Astronomy & Astrophysics

The GAPS Programme at TNG

LIV. A He I survey of close-in giant planets hosted by M-K dwarf stars with GIANO-B[★]

G. Guilluy[1], M. C. D'Arpa[2,3], A. S. Bonomo[1], R. Spinelli[2], F. Biassoni[4,5], L. Fossati[6], A. Maggio[2],
P. Giacobbe[1], A. F. Lanza[7], A. Sozzetti[1], F. Borsa[5], M. Rainer[5], G. Micela[2], L. Affer[2], G. Andreuzzi[8,9],
A. Bignamini[10], W. Boschin[8,11,12], I. Carleo[11,12], M. Cecconi[8], S. Desidera[13], V. Fardella[2,3], A. Ghedina[8],
G. Mantovan[13,14], L. Mancini[1,15,16], V. Nascimbeni[13], C. Knapic[10], M. Pedani[8], A. Petralia[2],
L. Pino[17], G. Scandariato[7], D. Sicilia[7], M. Stangret[13], and T. Zingales[13,14]

(Affiliations can be found after the references)

ABSTRACT

Context. Atmospheric escape plays a fundamental role in shaping the properties of exoplanets. The metastable near-infrared (nIR) helium triplet at 1083.3 nm (He I) is a powerful proxy of extended and evaporating atmospheres.

Aims. We used the GIARPS (GIANO-B + HARPS-N) observing mode of the Telescopio Nazionale *Galileo* to search for He I absorption in the upper atmospheres of five close-in giant planets hosted by the K and M dwarf stars of our sample, namely WASP-69 b, WASP-107 b, HAT-P-11 b, GJ 436 b, and GJ 3470 b.

Methods. We focused our analysis on the nIR He I triplet, performing high-resolution transmission spectroscopy by comparing the in-transit and out-of-transit observations. In instances where nightly variability in the He I absorption signal was identified, we investigated the potential influence of stellar magnetic activity on the planetary absorption signal by searching for variations in the Hα transmission spectrum.

Results. We spectrally resolve the He I triplet and confirm the published detections for WASP-69 b (3.91 ± 0.22%, 17.6σ), WASP-107 b ($8.17^{+0.80}_{-0.76}$%, 10.5σ), HAT-P-11 b (1.36 ± 0.17%, 8.0σ), and GJ 3470 b ($1.75^{+0.39}_{-0.36}$%, 4.7σ). We do not find evidence of extra absorption for GJ 436 b. We observe night-to-night variations in the He I absorption signal for WASP-69 b, associated with variability in Hα, which likely indicates the influence of pseudo-signals related to stellar activity. Additionally, we find that the He I signal of GJ 3470 b originates from a single transit observation, thereby corroborating the discrepancies found in the existing literature. An inspection of the Hα line reveals an absorption signal during the same transit event.

Conclusions. By combining our findings with previous analyses of GIANO-B He I measurements of planets orbiting K dwarfs, we explore potential trends with planetary and stellar parameters that are thought to affect the absorption of metastable He I. Our analysis is unable to identify clear patterns, thus emphasising the necessity for additional measurements and the exploration of potential additional parameters that may be important in controlling He I absorption in planetary upper atmospheres.

Key words. methods: observational – techniques: spectroscopic – planets and satellites: atmospheres

1. Introduction

The atmospheres of exoplanets orbiting close to their host stars can be significantly influenced by stellar irradiation, which can cause the upper atmospheric layers to expand and, in some cases, even evaporate (e.g. Bourrier & des Etangs 2018). Atmospheric loss due to photo-evaporation could have played a roll in shaping the close-in exoplanets' demographics and could be responsible for both the Neptunian Desert (i.e. the dearth of planets with sizes between terrestrial and Jovian close to host stars; Lecavelier Des Etangs 2007; Davis & Wheatley 2009; Szabó & Kiss 2011; Beaugé & Nesvorný 2013) and the radius gap, which separates the dense super-Earths from the larger and puffier

mini-Neptunes (Fulton et al. 2017; Fulton & Petigura 2018). Pioneering investigations of atmospheric escape were carried out two decades ago (e.g. Vidal-Madjar et al. 2003, 2004). These studies focused on the Ly-α transition of hydrogen, which is the dominant element in hot gas giant atmospheres. The atomic hydrogen resulting from the thermal dissociation of H_2 absorbs the stellar X-ray and extreme ultraviolet (EUV; together XUV) radiation in the thermosphere, significantly increasing the local temperature; this then can lead to atmospheric expansion and escape. However, Ly-α observations are contaminated by both interstellar medium (ISM) absorption and geocoronal emission, which pose challenges to the interpretations of the observations.

Seager & Sasselov (2000) and Oklopčić & Hirata (2018) identified the He I 2^3S triplet at 1083.3 nm (referred to as He I) as a robust diagnostic for studying atmospheric expansion and possibly mass loss. This tracer resides in a region of the near-infrared (nIR) spectrum affected by neither ISM nor geocoronal emissions. Since the groundbreaking discovery of an extended
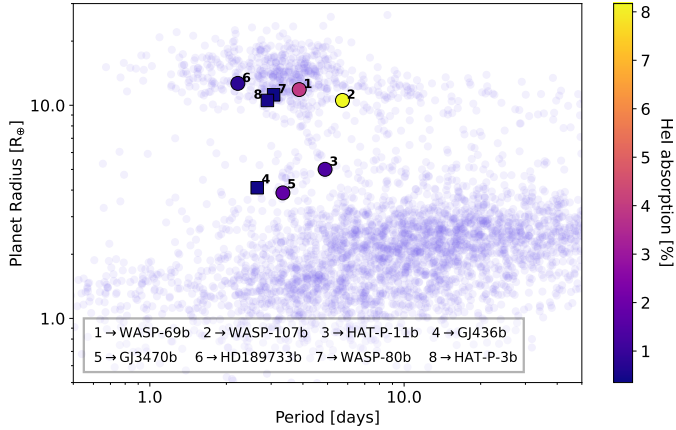

Fig. 1. Known exoplanets as a function of their radius and period from the NASA Exoplanet Archive (Akeson et al. 2013). Targets analysed in this work and previous GIANO-B papers (Guilluy et al. 2020, 2023; Fossati et al. 2022) are highlighted. The marker colour reflects the He I absorption signal we found in this work. Circles and squares represent detections and non-detections, respectively. The non-detections are reported at the 1σ level.

atmosphere surrounding the super-Neptune WASP-107 b (Spake et al. 2018), the field has made tremendous strides, with nearly 40 planets having been searched for the presence of He I to date (Dos Santos 2023). However, despite this large sample, the underlying factors responsible for triggering the detection or non-detection of He I remain unclear. Being aware of the potential limitations arising from differences in instrumentation and data analysis techniques that may affect the identification of trends related to He I detection, we decided to undertake a uniform survey, searching for He I in the atmospheres of all the exoplanets available within the atmospheric sample of the Global Architecture of Planetary Systems (GAPS) project (we described our GAPS-ATMO sample in Guilluy et al. 2022), which includes hot and warm Jupiter- and Neptune-like planets.

We divided the GAPS targets into two distinct subsamples. The first sample comprises planets orbiting M-K dwarf planet hosts, which we analyse in this paper. The second dataset, consisting of planets around G-F-A main-sequence stars, will be the subject of a future study (Guilluy et al., in prep.). We decided to focus this first paper on M-K dwarf stars as they are the best suited to host planets with an escaping He I atmosphere. Indeed, their high XUV flux ionises the He I ground state, which, recombining, populates the metastable 2^3S ground level (from which the 1083.3 nm absorption originates), and their moderately low mid-UV flux prevents the 2^3S ionisation (e.g. Oklopčić 2019; Biassoni et al. 2024).

Past observations have revealed that stellar activity can contaminate He I measurements, leading to inaccurate estimations of He I absorption and the mass-loss rate (e.g. Salz et al. 2018; Guilluy et al. 2020). Specifically, the plage-like active regions are darker than the rest of the stellar disc in the helium channel; a planet transiting over quiescent regions of the star would enhance the contribution of active regions to the observed flux, resulting in a stronger absorption at 1083.3 nm. Conversely, if the planet obscures an active region, the net effect would be a reduction in He I absorption. One approach to addressing these pseudo-signals is to simultaneously monitor stellar activity diagnostics in the optical (such as Hα, Ca II H&K, and Na I) that exhibit an opposite behaviour compared to He I (Guilluy et al. 2020).

In this paper we present an investigation of the upper atmosphere of WASP-69 b, WASP-107 b, HAT-P-11 b, GJ 436 b, and GJ 3470 b (see Fig. 1) using high spectral resolution observations in both the nIR with GIANO-B (Oliva et al. 2006) and in the optical using the High Accuracy Radial velocity Planet Searcher for the Northern hemisphere (HARPS-N; Cosentino et al. 2012) spectrographs.

The paper is organised as follows. We describe the sample in Sect. 2 and the observations in Sect. 3. We detail the data reduction procedures in Sect. 4. We highlight our findings and place our results in the context of previous works in Sect. 5. We finally draw our conclusions in Sect. 6.

2. Case history

Our survey encompasses five targets, namely WASP-69 b, WASP-107 b, HAT-P-11 b, GJ 436 b, and GJ 3470 b. In this section, we provide a brief overview of the key characteristics of each system and summarise the existing He I studies presented in the literature. The stellar and planetary parameters we adopted in the analysis are reported in Table A.1.

WASP-69 b is a warm Saturn orbiting a K5 star (Anderson et al. 2014). Due to its large expected atmospheric signal $2R_P H_{eq}/R_\star^2 \sim 283$ ppm (where H_{eq} is the atmospheric scale height, and R_P and $R_\star$ are the planetary and stellar radius, respectively, Brown et al. 2001), WASP-69 b represents a prominent target for performing atmospheric studies. Tsiaras et al. (2018) and Estrela et al. (2021) found clues to the presence of water in the planet's atmosphere. We recently reported the presence of five molecules, and a possible hint of disequilibrium in its lower atmosphere (Guilluy et al. 2022). Sodium was also detected in its upper atmosphere (see e.g. Casasayas-Barris et al. 2017; Khalafinejad et al. 2021; Langeveld et al. 2022). Evidence of an extended helium atmosphere surrounding the planet has been reported by Nortmann et al. (2018) with CARMENES, by Vissapragada et al. (2020, 2022) with Palomar/WIRC, by Allart et al. (2023) with SPIRou, and by Tyler et al. (2024) with Keck/NIRSPEC.

WASP-107 b is a super Neptune orbiting a K6 star located at the upper radius border of the Neptunian desert (Anderson et al. 2017). Because of its large atmospheric scale height, it represents an excellent target for atmospheric studies. Kreidberg et al. (2018) detected water using the Wide Field Camera 3 (WFC3) of the *Hubble* Space Telescope (HST), finding evidence for a methane-depleted atmosphere and high-altitude condensates. Spake et al. (2018) also detected water using a wider wavelength coverage than Kreidberg et al. (2018). Recently, photochemically produced sulphur dioxide (SO_2) was detected in its atmosphere (Dyrek et al. 2024). Detections of the extended helium atmosphere of WASP-107 b have been reported multiple times (e.g. Spake et al. 2018, 2021; Allart et al. 2018; Kirk et al. 2020).

HAT-P-11 b is a transiting warm Neptune-class exoplanet orbiting a K4V star, and located at the edge of the evaporation desert Bakos et al. (2010). Fraine et al. (2014), Tsiaras et al. (2018), and Chachan et al. (2019) detected the presence of water vapour in the atmosphere of HAT-P-11 b with low-resolution observations by using data from HST and *Spitzer*. Chachan et al. (2019) also suggested the presence of methane. More recently, at high-spectral resolution Basilicata et al. (2024) reported the detection of H_2O, NH_3, and a tentative one of CO_2 and CH_4. Ben-Jaffel et al. (2022) by studying the upper atmosphere found a phase-extended transit absorption of

neutral hydrogen and singly ionised carbon, while several works (i.e. Allart et al. 2018, 2023; and Mansfield et al. 2018) reported the presence of metastable helium surrounding the planet.

GJ 436 b is a warm Neptune in the lower-mass edge of the Neptune desert orbiting a quiet M2.5V star Gillon et al. (2007). Its atmosphere has been extensively studied through various observations. According to low-resolution studies, there appears to be a scarcity of methane and a surplus of CO and CO_2 in the atmosphere, along with a slight deficiency of H_2O when compared to the predicted amounts based on equilibrium chemistry assuming solar metallicity (e.g. Stevenson et al. 2010; Knutson et al. 2014). Observations of the upper atmosphere of GJ 436 b n Ly-α line of neutral hydrogen revealed that the planet is surrounded by a giant coma of H I extending tens of planetary radii (e.g. Kulow et al. 2014; Ehrenreich et al. 2015; Lavie et al. 2017), while Nortmann et al. (2018) did not detect any evidence of a helium-extended atmosphere.

GJ 3470 b is a warm Neptune orbiting an M-dwarf and located very close to the Neptunian desert (Bonfils et al. 2012). Previous investigations of its atmosphere, based on observations from the HST, have indicated the presence of a cloudy, hydrogen-rich atmosphere (Ehrenreich et al. 2014). Additionally, studies analysing visible range observations by Nascimbeni et al. (2013) and Chen et al. (2017) have detected a Rayleigh slope in the atmosphere. Benneke et al. (2019) obtained a robust detection of water absorption (>5σ) by combining HST and *Spitzer* observations. They revealed a low-metallicity, hydrogen-dominated atmosphere similar to a gas giant, but strongly depleted in methane gas. In terms of upper atmospheric layers, Bourrier et al. (2018) have reported the existence of a giant hydrogen exosphere while Palle et al. (2020) and Ninan et al. (2020) have identified evidence of He I absorption during transit. On the other hand, Allart et al. (2023) have reported a non-detection of He I in this planet's atmosphere.

3. Observations

The systems in our sample were observed using the GIARPS observing mode (Claudi et al. 2017) of the Telescopio Nazionale *Galileo* (TNG). In this configuration, the TNG is capable of simultaneously acquiring high-resolution (HR) spectra in the optical range (0.39–0.69 μm) and nIR range (0.95–2.45 μm) using the HARPS-N ($R \approx 115\,000$) and GIANO-B ($R \approx 50\,000$) spectrographs.

For the GIANO-B observations, we employed an ABAB nodding pattern, which allows for optimal subtraction of thermal background noise and telluric emission lines. Each target was scheduled for observations ~1 h before, during, and ~1 h after the planetary transit. Figure A.1 displays the signal-to-noise ratio (S/N) averaged over the region of interest (1082.49–1085.5 nm) and the airmass as a function of the planet's orbital phase for each night and target considered. GIANO-B covers four spectral bands in the nIR (Y, J, H, and K) divided into 50 orders. For our analysis, we focused on order #39 in the Y-band, where the He I triplet is located. One transit observation of WASP-69 b on UT 28 October 2021, was affected by thin clouds (cirri), prompting us to discard the AB pairs of observations with very low S/N compared to the others (lowest S/N in the pair less than 15, as shown in Fig. 2 of Guilluy et al. 2022). Furthermore, we discarded the last transit of WASP-107 b, which took place on UT 09 April 2023, as the entire night was affected by seeing conditions of approximately 2 arcseconds. This resulted in a lower S/N compared to the data from the other observing nights (see

Fig. A.1), thereby preventing us from analysing this dataset. A detailed log of the GIANO-B observations is provided in Table 1.

The HARPS-N observations were carried out using the objAB observational setup, with fibre A on the target and fibre B on the sky. The light collected through the fibres is directed to a 4k × 4k charge-coupled device (CCD). The CCD is responsible for capturing the spectra from 69 different orders for each fibre, utilising the echelle spectrograph design. To process the HARPS-N data, the standard Data Reduction Software (DRS) was employed, specifically version 3.7 (Cosentino et al. 2012).

4. Data analysis

In this section, we discuss the main steps of the analysis we performed on both GIANO-B (Sect. 4.1) and HARPS-N data (Sect. 4.2).

4.1. Analysis in the nIR

Currently, the most widely used technique for determining whether an exoplanet is surrounded by an extended or evaporating atmosphere is transmission spectroscopy. During a transit, the outgassed atoms produce additional absorption features superimposed on the stellar spectrum. Here, we outline the procedures we implemented to extract the planetary transmission spectra from the raw data obtained by GIANO-B.

4.1.1. Spectra extraction

We applied several data processing steps to the GIANO-B raw data using the GOFIO pipeline (Rainer et al. 2018). These steps included dark subtraction, flat field correction, removal of bad pixels, spectra extraction (without considering the blaze function correction), and wavelength calibration using a U-Ne lamp spectrum as a template in the vacuum wavelength frame. We used the ms1d spectra, the multi-spectral 1D output, where the echelle orders are kept separated. To improve the initial wavelength solution, we employed the same approach described in our previous works (e.g. Giacobbe et al. 2021; Guilluy et al. 2022). We aligned all the spectra to the Earth's atmospheric rest frame, assuming it as the frame of the observer (neglecting any ~10 m s^{-1} differences due to winds), by measuring any shifts relative to an average spectrum taken as a template for the night. Subsequently, we refined the wavelength solution by utilising an Earth's atmospheric transmission spectrum generated using the Sky Model Calculator[1].

For the remaining analysis, we focused exclusively on the order #39, which encompasses the He I triplet. The magnitude of these wavelength calibration refinements, for the considered nights and in the region around the He I triplet, is ~0.7 km s^{-1}, approximately one-fourth of a pixel.

4.1.2. Telluric correction

As our spectra were obtained from ground-based observations, it was necessary to account for the contribution of Earth's atmosphere. The telluric spectrum contains both emission and transmission lines. To correct for the transmission telluric lines, particularly the H_2O line at around 1083.51 nm (vacuum wavelength), we followed the approach proposed by Guilluy et al. (2023) and utilised the `Molecfit` ESO software

---

[1] https://www.eso.org/observing/etc/bin/gen/form?INS.MODE=swspectr+INS.NAME=SKYCALC

Table 1. Observations log.

	Date[(+)]	N_{obs}	Exp time [s]	S/N_{avg}	σ_{T_c} [min]	Telluric/stellar flag
WASP-69 b	24 July 2019	60	200.0	53.42	0.62	✓
	09 August 2020	54	200.0	54.39	0.72	
	28 October 2021	46	200.0	41.90	0.85	✓
	14 September 2022	42	200.0	51.88	0.95	
WASP-107 b	07 February 2019	58	200.0	28.21	0.24	
	04 May 2019	60	200.0	24.55	0.26	✓
HAT-P-11 b	07 July 2019	60	200.0	59.31	0.15	
	18 June 2020	60	200.0	65.22	0.16	
	19 September 2020	58	200.0	60.79	0.17	
GJ-436b	16 April 2018	44	200.0	67.34	0.17	
	19 February 2020	38	200.0	87.39	0.20	
	27 February 2020	38	200.0	93.26	0.20	
	03 March2023	30	200.0	78.45	0.24	
	11 March2023	46	200.0	90.75	0.24	
	24 December 2022	42	200.0	81.61	0.25	
GJ-3470b	13 January 2018	38	200.0	20.16	0.27	✓
	04 February 2019	52	200.0	21.41	0.32	✓
	28 December 2019	64	200.0	31.23	0.36	
	27 January 2020	48	200.0	36.26	0.36	✓
	23 December 2022	54	200.0	32.59	0.49	

Notes. From left to right: the observing night, the number of observed spectra, the exposure time, the average S/N across the selected spectral range (1082.49–1085.5 nm), the uncertainty on the mid-transit time for the observed transits calculated as $\sigma_{T_c} = \sqrt{\sigma_{T_0}^2 + n^2 * \sigma_P^2}$ (where T_0 and P are the mid-transit time and orbital period in the adopted ephemerids reported in Table A.1 and n is the number of orbits between times T_c and T_0), and flag for significant telluric overlap/possible stellar activity issues. [(+)]Beginning of the night.

(Smette et al. 2015; Kausch et al. 2015). An example of telluric removal is shown in the right panels of Fig. 2.

Within the spectral region of interest, there are two OH emission line doublets located close to the He I triplet. The first doublet is at approximately 1083.2103 nm, and 1083.2411 nm, while the second one is at 1083.4241 nm and 1083.4338 nm in vacuum wavelengths (Oliva et al. 2013). The GIANO-B resolving power is not able to distinguish between the two separate components of this second doublet, resulting in them being observed as a single, intense line in the spectra. The GIANO-B nodding acquisition mode automatically corrects for these emission lines, as described in Guilluy et al. (2020). However, due to variations in atmospheric seeing during the observing nights, the A-B subtraction may leave residual signals at the deepest OH doublet (i.e. around 1083.43 nm, as seen in the left panels of Fig. 2). To account for this, we visually inspected the GIANO-B raw spectra to identify the location of this OH line in our spectrograph and created a mask to exclude any possible residuals from our final transmission spectra (Guilluy et al. 2023).

4.1.3. Transmission spectra calculation

To separate the stellar contribution from the potential planetary signal, we took the following steps:

(i) First, we shifted the spectra into the star rest frame using Eq. (1) from Guilluy et al. (2023) and the parameters listed in Table A.1. As depicted in the right panels of Fig. 2, the He I triplet lines align in the stellar rest frame.

(ii) Next, we normalised each spectrum to the continuum by dividing it by its median value (neglecting the spectral region around the He I triplet), excluding spectra with significantly lower S/Ns compared to the other exposures.

(iii) We created a master-out stellar spectrum, $S_{out}(\lambda)$, by averaging the out-of-transit spectra (i.e. with an orbital phase smaller than t_1 or greater than t_4[2]). Individual transmission spectra, $T(\lambda, i)$, were derived by dividing each spectrum by $S_{out}(\lambda)$.

(iv) Finally, we linearly interpolated the transmission spectra in the planet's rest frame using Eq. (2) from Guilluy et al. (2023). Figure 3 displays an example of the transmission spectroscopy 2D maps in the planet's rest frame for each planet, while the 2D maps for all the investigated nights are presented in Fig. A.2. For each investigated planet and each observed night, we then derived the fully in-transit transmission spectrum in the planet's rest frame T_{mean}, which is computed by averaging the transmission spectra with an orbital phase between t_2 and t_3. We did not consider the influence of centre-to-limb variations (CLVs) or the Rossiter-McLaughlin (RM) effect as previous studies have indicated a minimal impact on the He I (e.g. Allart et al. 2018, 2019; Nortmann et al. 2018).

To estimate the contrast c of the excess absorption at the position of the He I triplet, we fitted a Gaussian profile to each individual in-transit mean transmission spectrum with the differential evolution (DE) Markov chain Monte Carlo (MCMC; Ter Braak 2006) method, varying the peak position, the full-width half maximum (FWHM), the peak value (c), and an offset for the continuum. Correlated noise in the transmission spectra (mainly caused by systematic effects such as fringing, variations in the instrumental profile, changes in the position of the star in the slit, etc) was modelled through the Gaussian process (GP) regression within the same DE-MCMC tools, using a covariance

---

2 For those planets where there was a hint of a tail we discarded the corresponding spectra to compute the master stellar spectrum.
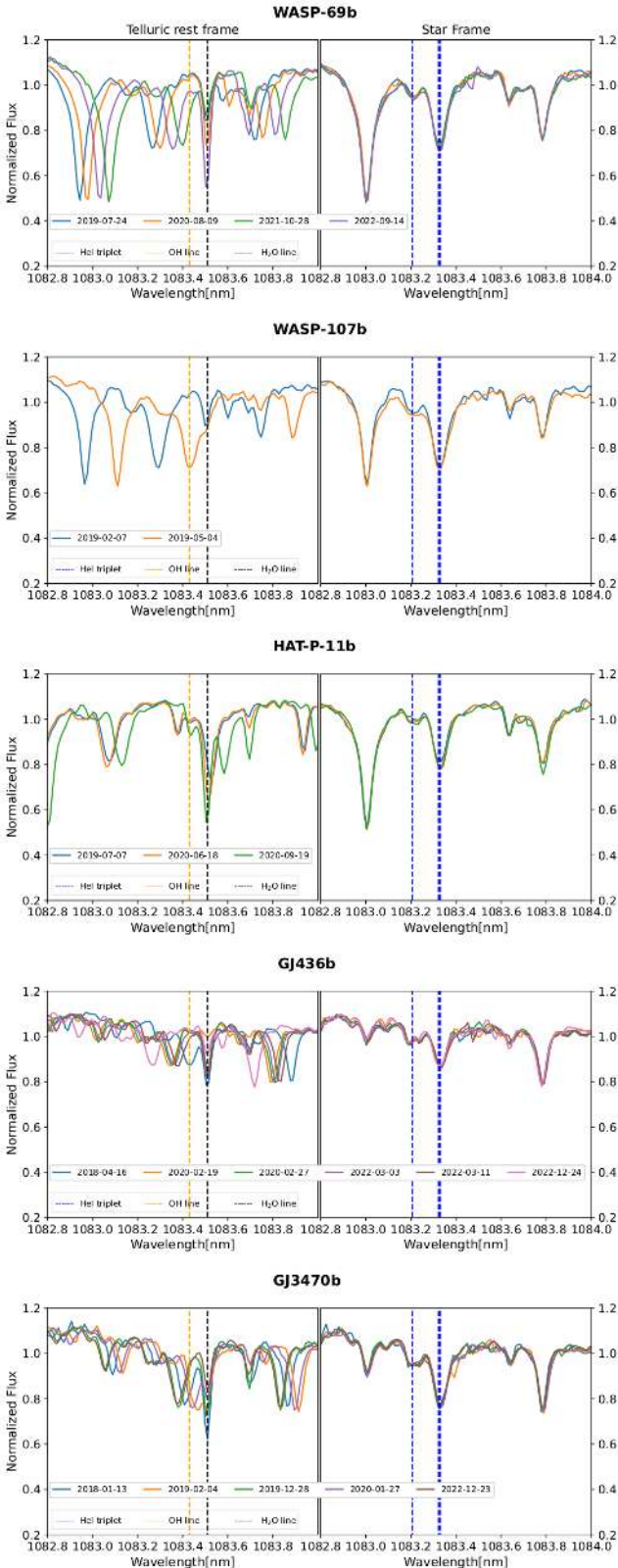
Fig. 2. Time-averaged spectra before and after the telluric lines removal. Left panels: averaged spectrum for each investigated night in the telluric rest frame, with the position of the H_2O telluric transmission line at ~1083.51 nm and the OH telluric emission line at ~1083.43 nm overplotted in black and orange, respectively. Right panels: averaged spectrum for each investigated night after the telluric removal and the shift in the stellar rest frame. Vertical blue lines correspond to the He I triplet. The averaged spectra are plotted after being divided by their median value for visualisation purposes.

matrix described by a squared exponential kernel (see Eq. (2) in Bonomo et al. 2023)[3]. We finally accounted for possibly uncorrelated noise with a jitter term σ_{jit}. We imposed several priors on the model parameters as well as on the GP hyper-parameters (see Table A.2). For each target, Fig. 4 shows an example of correction with the GP regression model, the posterior distributions for the same nights are reported in Fig. A.4. The best-fit parameters from the DE-MCMC Gaussian analysis, for each night are listed in Table A.3. We determined the values and the 1σ uncertainties of the derived parameters from the medians and the 16%-84% quantiles of their posterior distributions. In cases of a He I non-detection, we reported 1σ upper limits on the excess absorption at the positions of the stellar He I lines (Guilluy et al. 2023).

For each investigated target, the transmission spectra from each night were then weight-averaged after subtracting the GP regression model to create the final transmission spectra (see Fig. 5). Table 2 reports for each planet the weight-averaged He I contrast c.

4.1.4. Light-curve computations

To monitor the variation of the He I signal during transit, we additionally performed spectrophotometry of the helium triplet within a passband of 0.075 nm centred at the peak of excess absorption in the planet rest frame (Allart et al. 2019). The computed transit light curves are presented in Fig. A.3.

4.2. Analysis in the optical

To indicate the host star activity we derived the chromospheric emission from Ca II H&K lines of HARPS-N spectra ($\log R'_{HK}$). We used the definition of Noyes et al. (1984) and the implementation of Lovis et al. (2011) through the offline version of the HARPS-N DRS available through the Yabi workflow (Hunter et al. 2012) hosted at IA2 Data Center[4]. The only exceptions are GJ436 and GJ3470, for which the Noyes relations are not applicable as they have a colour index B-V > 1.1; we thus utilised the equations provided in Suárez Mascareño et al. (2015). The derived $\log R'_{HK}$ are reported in Table A.4.

We then derived transmission spectra in Hα similarly as described for the He I triplet. We focused on raw data already processed by the DRS and we used `Molecfit` to remove telluric contamination. We obtained transmission spectra (2D maps are in the upper panels of Figs. 6 and 7) by dividing the full in-transit spectra by the master out and we modelled CLVs and the RM effect similarly to Yan et al. (2017). However, instead of using models computed at different limb darkening angles μ, we used an analytical approach using ExoTethys (Morello et al. 2020) to retrieve the limb darkening coefficients and then computing the stellar intensity profile $I(\mu)$ by adopting a quadratic limb darkening law (D'Arpa et al. 2024). After shifting the transmission spectra into the planetary rest frame, we computed the weighted average of the full in-transit spectra (bottom-right panel of Figs. 6 and 7), and we fitted a Gaussian to evaluate the absorption/emission depth, FWHM, and the velocity shift. Along with the Gaussian fit, we also performed a linear fit and we computed the Bayesian information criterion (BIC)

---

[3] We also ran the DE-MCMC analysis without the GP, and our findings remain compatible within 1σ. However, the error bars on the model-free parameters (including the He I absorption) from the GP analysis are usually slightly larger, and thus more conservative, than those without the GPs, because they account for the correlated noise.
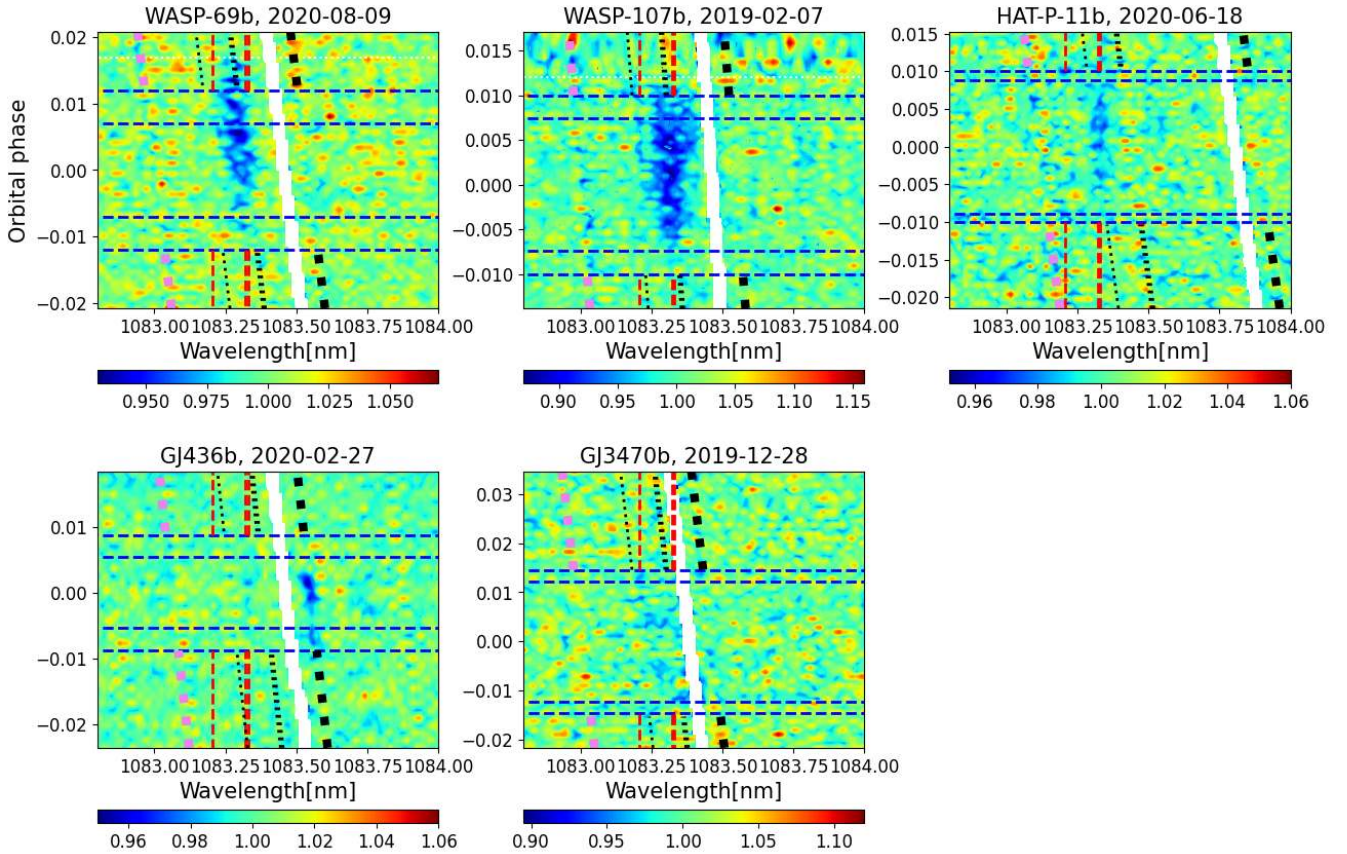
[4] https://www.ia2.inaf.it/

Fig. 3. 2D transmission spectra maps. For each target, an example of transmission spectra is shown in tomography in the planetary rest frame in the region of the He I triplet, as a function of wavelength and planetary orbital phase. The contact points t1, t2, t3, and t4 are marked with horizontal blue lines. The regions affected by OH contamination are masked. For some planets, some residuals are left at the position of the Si ~ 1083 nm line (highlighted in pink). This is due to the depth of the line (see e.g. Krishnamurthy et al. 2023; Zhang et al. 2023). Dotted black and red lines mark the position of the He I lines in the stellar and planet rest frame, respectively. Lines with black squares mark the position of the strong H_2O telluric line at around 1083.51 nm. The corresponding 2D maps for all the investigated nights are shown in Fig. A.2.

Table 2. Results combined.

Target	c [%]	Significance [σ]	Effective radius [R_p]	g_P [m s^{-2}]	H [km]	δ_{R_p}/H_{eq}
WASP-69 b	3.91 ± 0.22	17.6	1.79 ± 0.08	5.8 ± 0.6	1060	56 ± 8
WASP-69 b (without 24 July 2019)	3.46 ± 0.32	10.7	1.71 ± 0.08	5.8 ± 0.6	1060	51 ± 8
WASP-107 b (1 night)	$8.17^{+0.80}_{-0.76}$	10.5	2.19 ± 0.11	3.37 ± 0.31	1450	55 ± 7
HAT-P-11 b	1.36 ± 0.17	8.0	2.17 ± 0.11	10.2 ± 0.6	530	71 ± 9
GJ 436 b	$<0.42(0.52)^{(+)}$		$<1.27(1.33)$	14.8 ± 1.7	294	$<24(29)$
GJ 3470 b (1 night)	$1.75^{+0.39}_{-0.36}$	4.7	2.05 ± 0.25	8.2 ± 1.6	470	55 ± 19

Notes. From left to right: the investigated target, the contrast from the DE-MCMC analysis, the significance of the detection, the effective He I radius, the planet's gravity, the atmospheric scale height (computed by assuming a mean molecular weight of 1.3), and the ratio between the equivalent height of the He I atmosphere and the atmospheric scale height. $^{(+)}1\sigma(2\sigma)$ upper limits. For WASP-69 b, we also present results by excluding the first observing night (i.e. 24 July 2019), as it was likely affected by stellar contamination.

to compare the two models (Kass & Raftery 1995). We considered the Gaussian model as preferable over the linear one only when accompanied by a lower BIC and a difference in BIC (ΔBIC) > 10. We did not use the GP correction in the optical as the HARPS-N spectra are much less affected by systematics, and so the use of GPs was not really necessary.

5. Results

In this paper we performed a He I HR transmission spectroscopy survey of five gas giants namely WASP-69 b, WASP-107 b,

HAT-P-11 b, GJ 436 b, and GJ 3470 b. In this section, we summarise our findings. The last column of Table 1 highlights the nights with significant telluric overlap and possible stellar activity issues.

5.1. Individual analyses

5.1.1. WASP-69 b

We analysed four observing nights for WASP-69 b, namely 24 July 2019, 09 August 2020, 28 October 2021, and 14 September 2022. However, 28 October 2021 was affected by
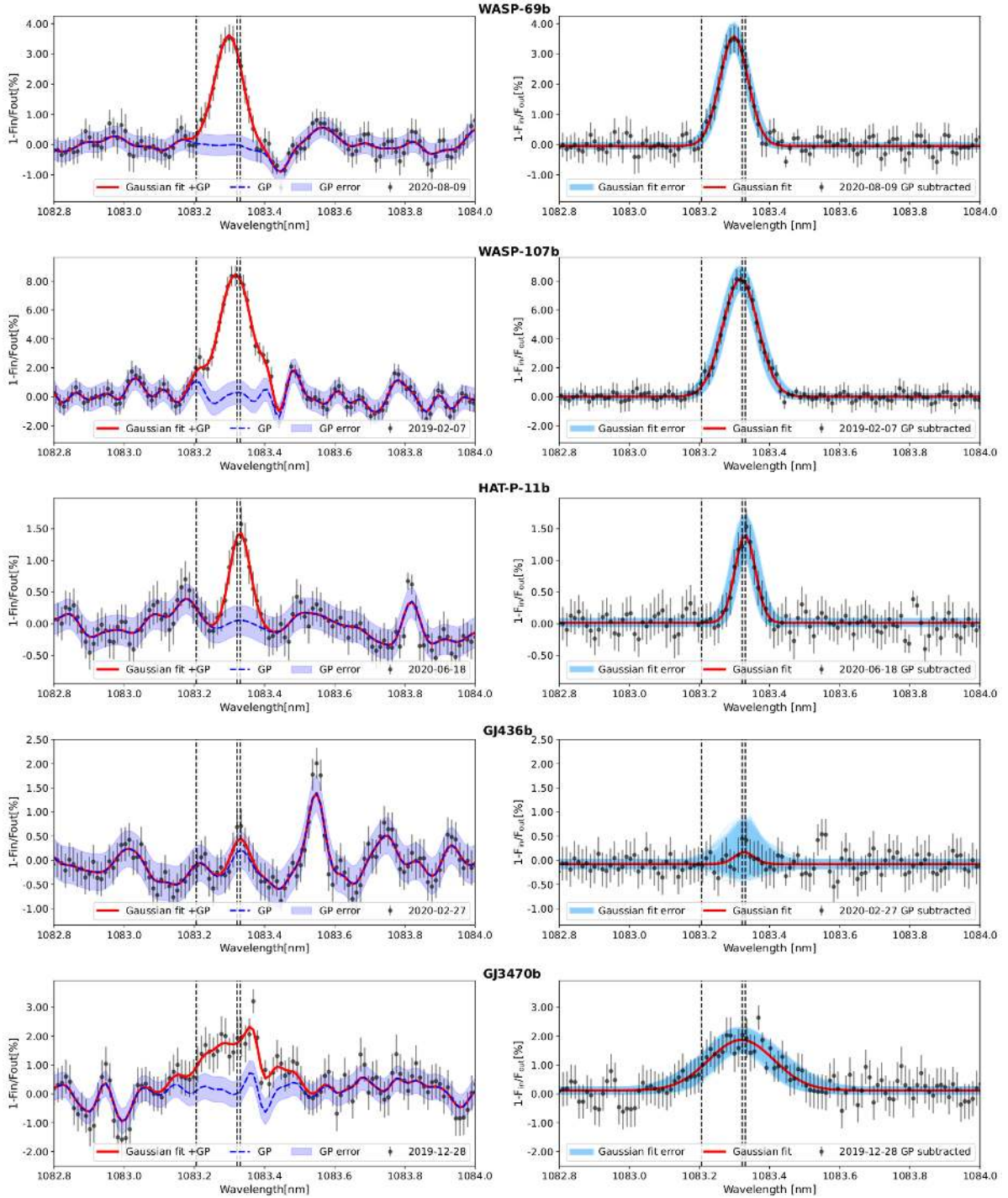
Fig. 4. GP correction. For each target, an example of GP correction is shown. Left panel: transmission spectrum centred on the He I triplet (in the planet rest frame) with overplotted the GP regression model, along with the 1σ uncertainty intervals, (in blue) and the Gaussian+GP model (in red). Right panel: final transmission spectrum after removing the GP model. Vertical black dotted lines indicate the position of the He I triplet. The spike in the right wing of the He I triplet in the GJ 3470 b transmission spectrum is a residual due to the OH emission line. The error intervals for the Gaussian fit were computed by displaying 1000 Gaussian fits within the 1σ uncertainties of the derived parameters, spanning the 16–84% quantiles.

OH contamination, we thus decided to exclude data from this night when computing the final contrast value[5]. We measured a contrast of 3.91 ± 0.22% (17.6σ), compatible with the value

reported by Nortmann et al. (2018), Vissapragada et al. (2020, 2022), and Tyler et al. (2024), while slightly higher than the one reported by Allart et al. (2023) with SPIRou (where they measured a maximum excess absorption of ~3.1%). From the 2D map in Fig. 3 we can confirm the existence of a cometary tail following the planet (Nortmann et al. 2018; Tyler et al. 2024). Our He I signal appears to persist for approximately ~50 minutes

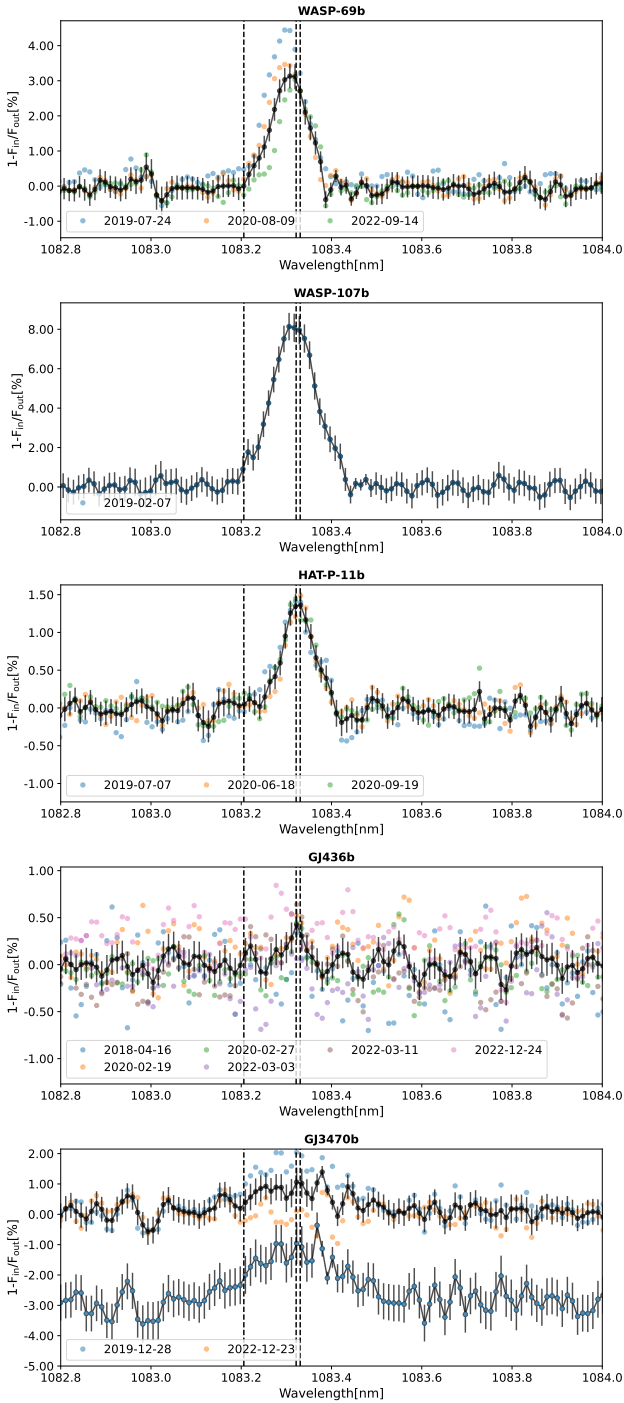_____

[5] When we also took into account that for 28 October 2021 an absorption signal of He I is still visible, albeit affected by OH contamination, in the 2D map in Fig. A.2, we measured a contrast of 3.88 ± 0.21% (18.8σ).

Fig. 5. Transmission spectra centred on the He I triplet (in the planet rest frame) after removal of the GP model. For each target, different colours refer to the different visits, and the black points show the weighted average over the observations. Vertical dotted black lines indicate the position of the He I triplet. For GJ 3470 b two different transmission spectra are reported, one by considering the two nights not affected by the OH contamination and one by considering only the night responsible for the He I signal. For WASP-69 b, the weighted averaged spectrum has been obtained by excluding the first night (i.e. UT 2019-07-24) as likely affected by stellar contamination.

after egress. Nortmann et al. (2018) reported a 22 min of post-transit absorption, while Tyler et al. (2024) observed a longer duration of 1.28 h after egress. The variations in tail lengths

might be attributed to intrinsic atmospheric variability or to insufficient baseline coverage and lower S/N in our study and Nortmann et al. (2018) compared to Tyler et al. (2024). From Fig. 5, UT 24 July 2019 appears to show a more pronounced absorption compared to the other transit events, with a compatibility of $\sim 1.9\sigma$ with the contrast value of $3.46 \pm 0.32\%$ (10.7σ) obtained by averaging the other three nights. We thus analysed the Hα diagnostic in the visible to investigate whether this disparity in the He I absorption levels was attributable to stellar contamination.

HARPS-N observations were available only for UT 24 July 2019 and UT 09 August 2020. Our findings are shown in Fig. 6, with the final transmission spectra in the bottom-right panel. For UT 09 August 2020, we obtained a BIC of 268.6 for the Gaussian fit and 269.8 for the linear fit, resulting in a ΔBIC of 1.8. According to Kass & Raftery (1995), the linear fit is the model that better describes our data, hence ruling out the presence of features in our transmission spectrum. This is also reinforced by the absence of features in the light curve shown in the bottom-left panel of Fig. 6. On the other hand, we detected an emission signal on UT 24 July 2019 ($1.45 \pm 0.19\%$, 7.6σ) for which the Gaussian fit was heavy favoured over the linear one (Gaussian BIC: 324.2, linear BIC: 352.2). Our detection is corroborated by the spectroscopic light curve, computed with a width of 20 km s^{-1}, which shows a clear emission feature during the first half of the transit (bottom-left panel of Fig. 6). This finding was further corroborated by the SLOPpy routine (Sicilia et al. 2022), which also revealed an excess of absorption during UT 24 July 2019 in the Sodium doublet (Sicilia et al., in prep.), in comparison to other nights.

This case appears similar to what was reported for HD 189733b in Guilluy et al. (2020) on the third night of observation, where an additional absorption in He I was observed in correspondence with an emission signal in Hα, suggesting that the planet was transiting over quiescent regions of the stellar surface. Given the activity of WASP-69 (as indicated by the $\log R'_{HK}$ measurements in Table A.4) we would expect to have a non-uniform stellar disc, and thus a possible occultation during the transit of quiescent stellar features. However, this signal appears redshifted in the stellar rest frame (17.4 ± 3.0 km s^{-1}; see Fig. A.5), while a pseudo signal caused by a plage-like region should be at rest in the star reference frame. An alternative explanation could be the presence of a flare. In this case, we would be observing the ejected material falling back to the star and hence moving away from us. This would account for the behaviour in He I and Hα, as well as the redshift in Hα in the stellar reference frame. The Hα line could be produced within a moving structure, for example, material falling towards the chromosphere or material moving away from us with the flare occurring near the edge of the star (thus explaining the redshift), while the He I absorption could be produced in a region outside the flare but irradiated by the XUV rays of the flare, which contribute to populating the atomic level from which the absorption that produces the line originates.

It is worth noting that Nortmann et al. (2018) also reported significantly different depths in the two CARMENES nights analysed in their study. This raises the question of whether a similar mechanism might be at play in their data.

In Fig. 3, the He I signal appears to be slightly tilted, indicating a different atmospheric K_P compared to the one obtained from the radial velocity curves (see Table A.1). We investigated a lag vector corresponding to possible atmospheric K_P in the range $0 \le K_P \le 250$ km s^{-1}, in steps of 1 km s^{-1}. We considered the
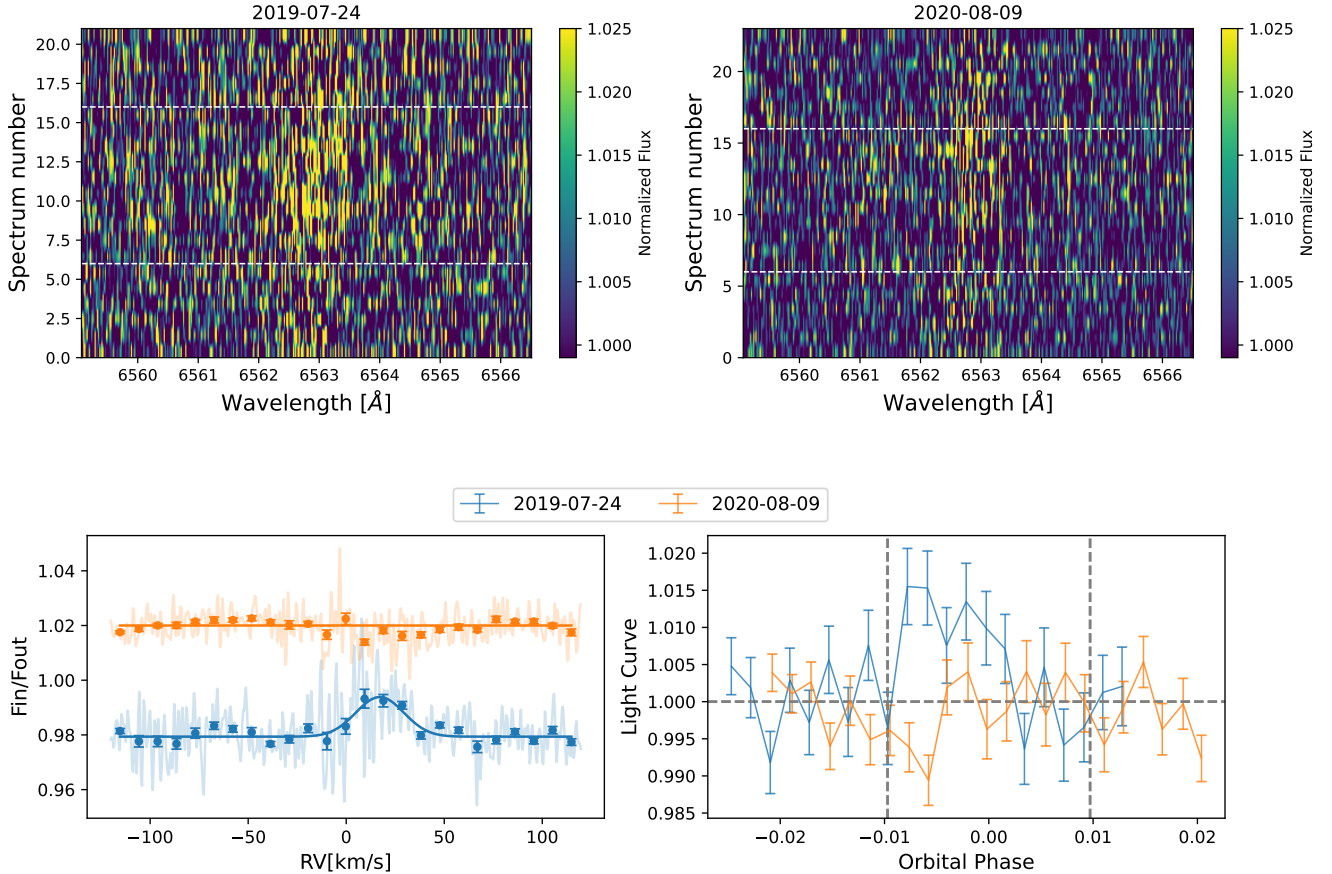
Fig. 6. Hα transmission spectra and light curves for WASP-69 b. Top: 2D transmission spectroscopy maps in the stellar rest frame for UT 24 July 2019 (top left) and UT 09 August 2020 (top right). Dotted red lines mark the position of the Hα line in the planet rest frame. Bottom: spectroscopic light curves (bottom left) and weighted average of the full in-transit spectra in the planet rest frame (bottom right; the equivalent in the stellar rest frame is in the left panel of Fig. A.5). Light colours indicate the not binned transmission spectra, while dots represent the transmission spectra binned 20 × (in RV). We superimposed the Gaussian profile derived from the best-fit parameters on the unbinned spectra.

two nights where the He I signal was less affected by the OH telluric emission line (i.e. UT 24 July 2019 and 09 August 2020). For each K_P value, we derived a 2D map (similar to those shown in Fig. 3) and a T_{mean} that we fitted with a Gaussian to determine the peak of He I absorption. We see that the He I absorption peak is maximised for an atmospheric K_P of approximately 80 km s^{-1} (lower than the one reported in the literature; see Table A.1). We have to stress that given the width of the single line we are investigating, this result has to be taken just as a maximisation but without any statistical significance. 3D hydrodynamic simulations suggest that the He I signal in robust outflows may not precisely follow the expected K_P. Once the gas starts getting outside the planetary Roche lobe the velocity dynamics can differ (see e.g. Nail et al. 2024 and Gully-Santiago et al. 2024).

5.1.2. WASP-107 b

We analysed two transits of WASP-107 b, 07 February 2019 and 04 May 2019. However, the second observing night was strongly affected by the OH emission line. If we consider only the first transit (i.e. UT 07 February 2019) we obtained an absorption of 8.17 $^{+0.80}_{-0.76}$% (10.5σ) compatible. If we consider only the first transit (i.e. UT 07 February 2019) we obtained an absorption of 8.17 $^{+0.80}_{-0.76}$% (10.5σ) compatible with 7.92 ± 1.00% and 7.26 ± 0.24% reported by Allart et al. (2019) and Kirk et al. (2020), respectively. Our 2D maps in Fig. 3 and the spectroscopic light

curve in Fig. A.3 indicate the possible presence of a tail following the planet, in agreement with Fig. 3 of Kirk et al. (2020) and Spake et al. (2021). However, our tail appears to be shorter than found in the latter study; this difference may be attributed to intrinsic atmospheric variability, as highlighted for WASP-69 b.

5.1.3. HAT-P-11 b

We gathered three transit observations for HAT-P-11 b. We reported an extra absorption of 1.36 ± 0.17% (8.0σ) in agreement with ∼1.2 and ∼1.3% reported by Allart et al. (2018) and Allart et al. (2023), respectively. According to Table A.3, all the helium absorption measurements are compatible within 0.5σ.

5.1.4. GJ 436 b

We collected six transits of GJ 436 b. We did not report any He I extra absorption for GJ 436 b, as our findings are consistent with zero absorption. Neither the single nights taken individually (see Fig. 3) nor the light curve (see Fig. A.3) show evidence of helium absorption with a 1σ upper limits of 0.42% (0.52% at 2σ). The small He I feature in our final transmission spectrum (Fig. 5) could be due to correlated noise falling at the position of the stellar helium triplet not perfectly corrected with the GP regression model. Our result is in agreement with Nortmann et al. (2018), who did not find evidence of He I in the upper atmosphere of GJ 436 b (they reported a 90% confidence
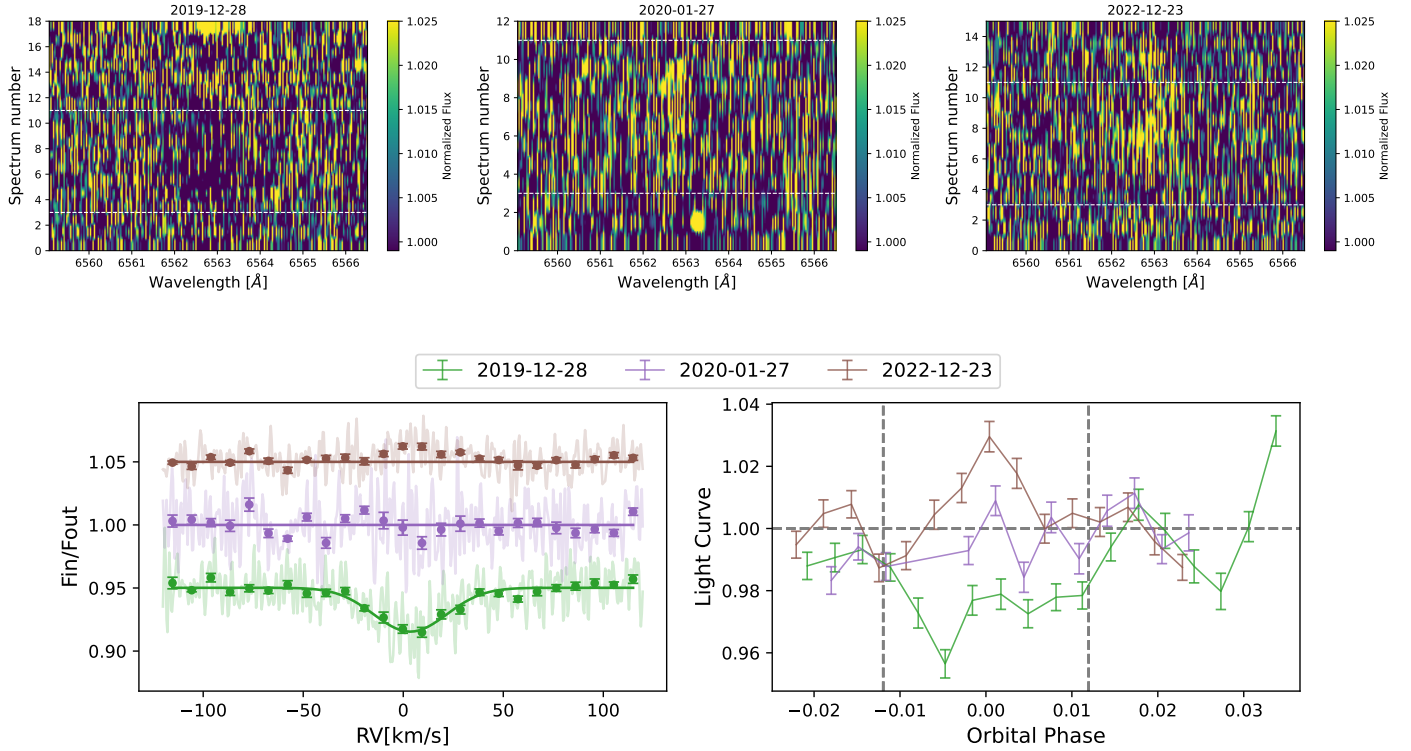
Fig. 7. Hα transmission spectra and light curves for GJ 3470b. Top: 2D transmission spectroscopy maps in the stellar rest frame for transit 3, transit 4, and transit 5 in panels a, b, and c, respectively. Dotted red lines mark the position of the Hα line in the planet rest frame. Bottom: spectroscopic light curves (panel d) and weighted average of the full in-transit spectra in the planet rest frame (panel e, the equivalent in the stellar rest frame is in the left panel of Fig. A.5).

upper limits of 0.41% calculated from the standard deviation of the spectrum).

5.1.5. GJ 3470 b

Here, we analysed five nights of observations, namely 13 January 2018, 04 February 2019, 28 December 2019, 27 January 2020, and 24 December 2022, which we refer to as transit 1, transit 2, transit 3, transit 4, and transit 5 for simplicity. As the 2D maps in Fig. 3 show, three (i.e. transit 1, transit 2, and transit 4) were strongly contaminated by the OH telluric emission line, we thus decided to discard these nights. The 2D maps (Fig. 3) suggest that the majority of the signal originates from transit 3. If we account for only this transit, we obtained a tentative detection of the extra absorption of $1.75^{+0.39}_{-0.36}$% (4.7σ), in agreement with Ninan et al. (2020), ~1.5% from their Fig. 5, and Palle et al. (2020), 1.5 ± 0.3%. Allart et al. (2023) could not replicate the detection with SPIRou and only placed a 3σ upper limit on the presence of helium at 0.63%. Despite our detection being consistent at 3σ with no absorption, tomography reveals a hint of absorption at the helium triplet position.

It is worth noting that Palle et al. (2020) observed variability across the analysed nights (see their Table 3) and attributed it to differences in the S/N. However, in our investigation, we find comparable S/N between transit 3 and transit 5. The tension in the literature is not so surprising, considering our result.

Given the lack of homogeneity in the He I observation across the various investigated nights, we also analysed the Hα line in a similar way to WASP-69 b (Fig. 7). Out of the five nights under consideration, only three were usable in terms of S/N, namely transit 3, transit 4, and transit 5. We identified an absorption signal (3.48 ± 0.26%, 13σ) at rest in the planet's reference frame

during transit 3 (as depicted in panels a and e of Fig. 7). The BIC analysis confirms the absorption signal detected with a BIC value of 401.5 for the Gaussian and 462.5 for the linear fit. This particular night contributed to the majority of the He I signal. If this simultaneous absorption signal in both He I and Hα was due to stellar activity, it could be explained by the planet's passage over a quiescent region of the stellar disc, during which time the star presents filaments. These regions being darker than the rest of the star in both helium and Hα could have caused this pseudo-signal in absorption in both the stellar lines. On the other hand, it is also plausible that the Hα absorption feature may be attributed to an extended planetary hydrogen atmosphere. However, theoretical transmission profiles simulated using the ATES code (Caldiroli et al. 2022) and the new add-on transmission probability module (Biassoni et al. 2024) are not able to reproduce an absorption depth/profile consistent with our observations. For this simulation, we assumed a local thermodynamic equilibrium (LTE) profile and adopted the X-ray luminosity of $\log(L_X) = 27.58$ measured by Spinelli et al. (2023) and two different X-ray-EUV relations, derived by Johnstone et al. (2021) and Sanz-Forcada (2022): $\log(L_{EUV}) = 27.98$ and $\log(L_{EUV}) = 28.40$, respectively. Although the Hα population process may not be in the LTE regime (e.g. García Muñoz & Schneider 2019; Huang et al. 2023), our ATES analysis and the detection in only one of the three HARPS-N nights, make the hypothesis of a stellar origin for the feature detected in Hα the most plausible. Further analyses that include more detailed radiative transfer models are needed to confirm this hypothesis.

Concerning transit 4 (shown in violet in Fig. 7), the one significantly impacted by the OH emission line in He I, the HARPS-N data were affected by both noise and systematics (as evident in both the light curve and the 2D maps in panels b and d

of Fig. 7) and we had to remove two spectra for which the telluric correction with `Molecfit` did not work resulting in an overcorrection. In this case, the linear fit is favourite with respect to the Gaussian one (BIC 462.5 vs. 447.4) consistently with the absence of features in the light curve. Hence, we do not detect any Hα signal in this night. Finally, during transit 5 (depicted in brown in Fig. 7), there appears to be an emission signal in Hα, as highlighted from both the 2D map (panel c) and the spectroscopy light curve (panel d). This signal seems more pronounced in the star's rest frame (right panel of Fig. A.5) even if with a low significance of $\sim 4\sigma$. Consequently, it may be attributed to stellar activity; for instance, the planet's transit over a dark region on the stellar disc, such as a filament, could potentially mimic a pseudo-signal in emission in both Hα and He I, thereby impacting our helium detection. However, considering the low significance of this detection, the small number of spectra (i.e. 15), and the moderate S/N (~ 38), we cannot dismiss the possibility that this result may be solely attributed to statistical noise. This hypothesis is supported by the BIC test, which returns the same value for both the linear fit and the Gaussian one (BIC = 398), suggesting that we should prefer the model with fewer parameters.

5.2. Statistical analyses

In this section, we looked for possible correlations between the He I absorption feature and the stellar and planetary parameters thought to be keys for the He I signal observability. To achieve this goal, in addition to the findings presented in this paper, we also considered previous He I studies performed with GIANO-B, namely HD 189733b (Guilluy et al. 2020), WASP-80 b (Fossati et al. 2022), and HAT-P-3b (Guilluy et al. 2023).

For each planet in our sample, we derived the effective He I radius (e.g. Chen et al. 2018) that would produce the observed absorption contrast c (see Table 2). We then normalised it to the atmospheric H_{eq} to compute the quantity δ_{R_P}/H_{eq} (Nortmann et al. 2018), which represents the number of scale heights probed by the atmosphere in the spectral range under consideration. Here, H_{eq} is defined as $\frac{k_B T_{eq}}{\mu g_P}$ (see Table 2), where k_B is the Boltzmann constant, T_{eq} is the planetary equilibrium temperature (listed in Table A.1), g_P is the planetary gravity calculated from the planetary mass and radius (see Table 2), and μ is the mean molecular weight. According to Fossati et al. (2022), we assumed a hydrogen-dominated atmosphere and hence $\mu = 1.3$ times the mass of a hydrogen atom (we opted for a hydrogen-dominated atmosphere rather than a hydrogen-and-helium atmosphere to mitigate uncertainties arising from the unknown helium abundance[6]). The derived δ_{R_P}/H_{eq} values for each investigated planet are presented in Table 2.

In Fig. 8, we examined how these derived constraints vary with respect to the EUV flux in the 200–504 Å range (which controls the He I metastable production, and therefore absorption, in the planetary atmosphere, Fossati et al. 2023), effective temperature, planetary gravity, and log R'_{HK}. We used the EUV flux derived in Fossati et al. (2023) from the scaling relations of Poppenhaeger (2022). We employed the same methodology to derive the EUV flux received by HAT-P-3b, the only one

---

[6] The value of $\mu = 1.3$ is typically considered for hot Jupiters assuming solar abundances, but it also takes into account the presence of a mix of molecular hydrogen and electrons resulting from the ionisation of various elements, especially Na and K. Hydrogen and helium abundances are not the only factor to consider. We would like to emphasise that the adopted μ does not alter the final outcome, and does not influence the presence or absence of correlations.

Table 3. Correlations between the investigated planetary and stellar parameters expected to influence the He I observability.

X, Y	ρ Spearman	Correlation strength	p-value
$F_{EUV}, \delta_{R_P}/H_{eq}$	0.0116 ± 0.0029	Null	0.98
F_{EUV}, c	0.1663 ± 0.0029	Low	0.69
$T_{eff}, \delta_{R_P}/H_{eq}$	-0.0302 ± 0.0028	Null	0.94
T_{eff}, c	-0.1665 ± 0.0027	Low	0.70
$g_P, \delta_{R_P}/H_{eq}$	0.0664 ± 0.0028	Null	0.88
g_P, c	-0.1886 ± 0.0026	Low	0.65
$\log R'_{HK}, \delta_{R_P}/H_{eq}$	-0.1303 ± 0.0028	Low	0.76
$\log R'_{HK}, c$	0.1461 ± 0.0030	Low	0.73

Notes. From left to right: the parameters investigated for the correlation, the Spearman value, the strength of correlation from Kuckartz et al. (2013), and the associated p-value.

missing in the sample analysed by Fossati et al. (2023). As no X-ray measurements were present in the literature, we estimated it starting from our derived log R'_{HK} value (see Table A.4) and the Mamajek & Hillenbrand (2008) relation, obtaining a value of $Lx = 1.3^{+2.2}_{-0.8} \, 10^{27}$ erg s^{-1}. We then employed the Poppenhaeger (2022) relations to estimate the EUV flux. However, due to the large uncertainty on the derived X-ray luminosity, we were unable to constrain the coronal temperature (relation from Johnstone & Güdel 2015). As a result, considering a range of 1.25–2.1 MK for the coronal temperature, we obtained two different EUV flux values using the scaling relations of Poppenhaeger (2022): 36 erg s^{-1} cm^{-2} and 1095 erg s^{-1} cm^{-2}.

Trends related to the contrast c and atmospheric extension δ_{R_P}/H_{eq} are shown in the left and right panels of Fig. 8, respectively. To evaluate the strength of the possible correlations between the investigated parameters, we ran an MCMC, varying the He I contrasts c according to a normal distribution with a standard deviation equal to the error we found on c. In the case of non-detection, we used a half-Gaussian distribution centred at zero with a standard deviation equal to the 1σ upper limit. We ran 10 000 iterations and at each MCMC step, we computed the Spearman rank-order correlation coefficient ρ to measure the strength of our relationships. The final mean values, the corresponding errors, and the p-values are reported in Table 3. The p-values were computed using a t-test under the null hypothesis that the correlation coefficients are significantly different from 0.

Our findings do not show significant correlations between the investigated parameters (p-values > 0.05). The null hypothesis that any two parameters X, Y in Table 3 are uncorrelated is rejected with a confidence level not exceeding 90%, corresponding to a <2σ result. However, it is important to underline that we are still within the statistical limit of small numbers, so the results should be interpreted with caution. Furthermore, it is important to underscore that there might be variability among planets, attributable in part to possible differences in helium abundance in the atmosphere. This variability could introduce additional noise, potentially hindering our ability to establish statistical correlations. Finally, H_{eq} might not be the correct physical length scale to consider in such an analysis. For instance, Zhang et al. (2023) showed that the scale height does not correlate with the contrast measured for the deepest individual lines in a sample of exoplanets, attributing this effect to hydrodynamical effects arising in the upper part of the atmosphere. Even within the hydrostatic region of an atmosphere, in the presence of significant variations with altitude of
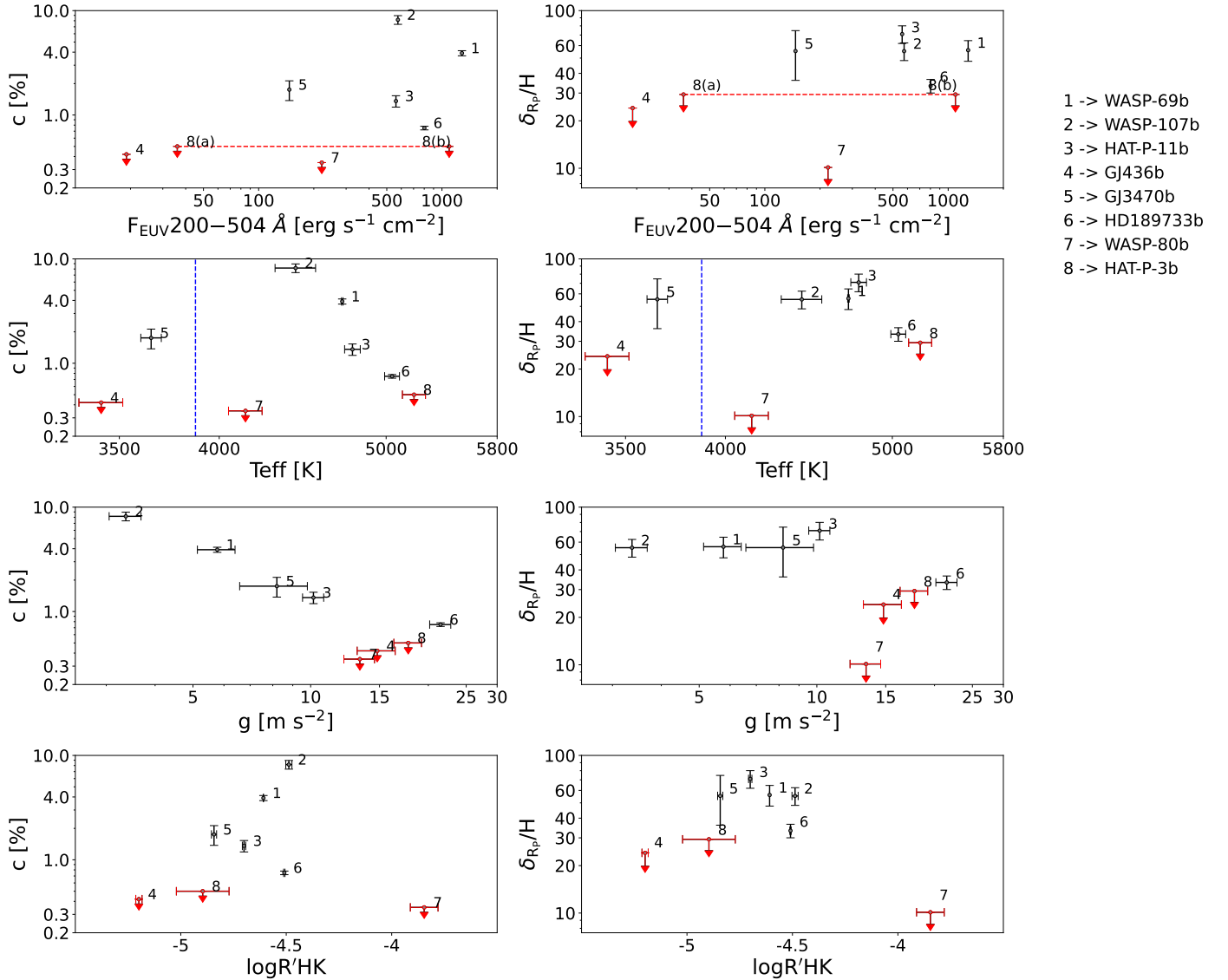
Fig. 8. Correlation plots. Targets are from this work, Guilluy et al. (2020, 2023), and Fossati et al. (2022). Contrast c (left panels) and δ_{R_P}/H_{eq} (right panels) as a function of the EUV flux in the 200–504 Å range, effective temperature and planetary gravity, and $\log R'_{HK}$. Red markers indicate targets with only an upper limit on the He I detection (reported at 1σ). The vertical dashed blue lines in the effective temperature diagrams indicate the transition from M-type to K-type stars. The dashed horizontal line connects the two possible locations for HAT-P-3b (for the two different coronal temperatures).

temperature, gravity or even mean molecular weight, using a single scale height might be too simplistic.

These potential trends do not highlight any explanations that could justify the detection and non-detection of metastable He I in the upper atmospheres of the investigated planets[7]. The three planets with only upper limits on the He I detection, namely GJ 436 b, WASP-80 b, and HAT-P-3 b do not seem to exhibit a clear correlation in the investigated parameter space. Fossati et al. (2023) emphasised that the low-EUV stellar flux, influenced by the low [Fe/O] coronal abundance (Poppenhaeger 2022), is likely the primary factor behind the He I non-detection. Rumenskikh et al. (2023) attributed the weak He I signature reported by Nortmann et al. (2018, 0.41%, 2σ) to the thinness

of the region populated by the absorbing He I ($<3R_P$), the small $R_P/R_\star$ ratio, and the radiation pressure force, which spreads He I atoms along the line of sight and around the planet. Yet, there is still no explanation for the non-detection in the atmosphere of HAT-P-3b.

It is interesting to highlight that both HAT-P-3 b and GJ 436 b are on a polar orbit with a 3D true obliquity (ψ) of $75.7^{+8.5}_{-7.9}$ deg (Bourrier et al. 2023) and $103.2^{+12.8}_{-11.5}$ deg (Bourrier et al. 2022), respectively. On the other hand, WASP-80 b is well known to be on a relatively aligned orbit (Triaud et al. 2015). This may indicate that also the orbital obliquity does not influence the He I observability.

It is important to note that in our study, in Fossati et al. (2022), and in Guilluy et al. (2020), we analysed multiple transit events for each planet, investigating the repeatability of the He I signal. However, this is not the case for HAT-P-3b, as in Guilluy et al. (2023) only one night of observation was gathered

---

[7] The results remain consistent when we consider the contrast c (and the corresponding δ_{R_P}/H_{eq}) obtained by excluding the night of UT 24 July 2019 for WASP-69 b, likely affected by stellar contamination.

and examined. Therefore, obtaining more data is essential to provide clarity on this non-detection.

6. Summary and conclusion

We employed the GIARPS mode of the TNG, focusing on GIANO-B observations to look for He I in the upper atmosphere of five planets hosted by the K and M dwarf stars of our sample, namely WASP-69 b, WASP-107 b, HAT-P-11 b, GJ 436 b, and GJ 3470 b. We measured a contrast, c, of the excess absorption of $3.91 \pm 0.22\%$ (17.6σ), $8.17^{+0.80}_{-0.76}\%$ (10.5σ), and $1.36 \pm 0.17\%$ (8.0σ) for WASP-69 b, WASP-107 b, and HAT-P-11 b, respectively, confirming the literature detections. Our analysis of WASP-69 b showed a night-to-night variability in the helium absorption levels, with the first transit exhibiting a higher absorption value compared to the others. We thus inspected the Hα line in HARPS-N spectra, finding an opposite behaviour in Hα compared to that recorded in He I on UT 29 July 2019. We interpreted this as being due to the effect of stellar activity, and we speculated on the possible origins of this effect.

We report a detection of He I in the upper atmosphere of GJ 3470 b of $1.75^{+0.39}_{-0.36}\%$ (4.7σ). Our result is in agreement with previous studies by Ninan et al. (2020) and Palle et al. (2020). However, if we consider only the two nights not affected by the OH emission line, the signal seems to appear from only one transit, supporting the literature discrepancy and indicating the presence of variability, whereby the extended atmosphere is more evident on certain nights than on others. Additional observations are needed to unveil the origin of the He I signal. An inspection of the Hα line reveals a hydrogen absorption signal during the same transit event. Our ATES simulations are not able to reproduce an absorption depth or profile consistent with our observations, thus making stellar activity the most plausible origin for this feature. Further analyses that include more detailed radiative transfer models are needed to confirm this hypothesis.

In agreement with previous work (Nortmann et al. 2018), we did not detect a He I excess of absorption for GJ 436 b. Our finding is compatible with zero absorption.

We finally placed our results in the context of other He I analyses of planets orbiting K- and MV-type stars obtained with GIANO-B, namely HD 189733b (Guilluy et al. 2020), WASP-80 b (Fossati et al. 2022), and HAT-P-3b (Guilluy et al. 2023). We explored potential trends associated with stellar and planetary parameters believed to influence the He I detection, such as the EUV flux, the effective temperature, the planet's gravity, and the $\log R'_{\rm HK}$. Our analysis does not show any significant correlation, and our investigation did not reveal any relationship between GIANO-B detections and non-detections in the atmospheres of planets around M-K dwarf stars and the parameters we explored. We emphasise that this could also be a consequence of our small sample size. Moreover, both the stellar EUV flux and the helium abundance in the investigated atmospheres are highly uncertain, which may introduce noise when attempting to identify potential correlations. Additional observations are thus needed, together with the investigation of new parameters that could influence the He I observability.

Our work underscores the importance of a He I survey homogeneous in both observation techniques and data analysis methods, both of which are essential to understanding the key parameters governing He I detectability. It also emphasises the necessity of simultaneous nIR and visible monitoring to investigate the potential presence of stellar activity pseudo-signals in He I measurements.

References

Akeson, R. L., Chen, X., Ciardi, D., et al. 2013, PASP, 125, 989
Allart, R., Bourrier, V., Lovis, C., et al. 2018, Science, 362, 1384
Allart, R., Bourrier, V., Lovis, C., et al. 2019, A&A, 623, A58
Allart, R., Lemée-Joliecoeur, P. B., Jaziri, A. Y., et al. 2023, A&A, 677, A164
Anderson, D. R., Collier Cameron, A., Delrez, L., et al. 2014, MNRAS, 445, 1114
Anderson, D. R., Collier Cameron, A., Delrez, L., et al. 2017, A&A, 604, A110
Bakos, G. Á., Torres, G., Pál, A., et al. 2010, ApJ, 710, 1724
Basilicata, M., Giacobbe, P., Bonomo, A. S., et al. 2024, A&A, 686, A127
Beaugé, C., & Nesvorný, D. 2013, ApJ, 763, 12
Ben-Jaffel, L., Ballester, G. E., Muñoz, A. G., et al. 2022, Nat. Astron., 6, 141
Benneke, B., Knutson, H. A., Lothringer, J., et al. 2019, Nat. Astron., 3, 813
Biassoni, F., Caldiroli, A., Gallo, E., et al. 2024, A&A, 682, A115
Biddle, L. I., Pearson, K. A., Crossfield, I. J. M., et al. 2014, MNRAS, 443, 1810
Bonfils, X., Gillon, M., Udry, S., et al. 2012, A&A, 546, A27
Bonomo, A. S., Dumusque, X., Massa, A., et al. 2023, A&A, 677, A33
Bourrier, V., & des Etangs, A. L. 2018, in Handbook of Exoplanets, eds. H. J. Deeg, & J. A. Belmonte (Berlin: Springer), 148
Bourrier, V., Ehrenreich, D., Allan, A., et al. 2018, A&A, 619, A1
Bourrier, V., Zapatero Osorio, M. R., Allart, R., et al. 2022, A&A, 663, A160
Bourrier, V., Attia, O., Mallonn, M., et al. 2023, A&A, 669, A63
Brown, T. M., Charbonneau, D., Gilliland, R. L., Noyes, R. W., & Burrows, A. 2001, ApJ, 552, 699
Butler, R. P., Vogt, S. S., Marcy, G. W., et al. 2004, ApJ, 617, 580
Caldiroli, A., Haardt, F., Gallo, E., et al. 2022, A&A, 663, A122
Casasayas-Barris, N., Palle, E., Nowak, G., et al. 2017, A&A, 608, A135
Chachan, Y., Knutson, H. A., Gao, P., & et al. 2019, AJ, 158, 244
Chen, G., Guenther, E. W., Pallé, E., et al. 2017, A&A, 600, A138
Chen, G., Pallé, E., Welbanks, L., et al. 2018, A&A, 616, A145
Claudi, R., Benatti, S., Carleo, I., et al. 2017, Eur. Phys. J. Plus, 132, 364
Cosentino, R., Lovis, C., Pepe, F., et al. 2012, SPIE Conf. Ser., 8446, 84461V
Cutri, R. M., Skrutskie, M. F., van Dyk, S., et al. 2003, VizieR Online Data Catalog: II/246
D'Arpa, M. C., Saba, A., Borsa, F., et al. 2024, A&A, submitted
Davis, T. A., & Wheatley, P. J. 2009, MNRAS, 396, 1012
Dos Santos, L. A. 2023, IAU Symp., 370, 56
Dyrek, A., Min, M., Decin, L., et al. 2024, Nature, 625, 51
Ehrenreich, D., Bonfils, X., Lovis, C., et al. 2014, A&A, 570, A89
Ehrenreich, D., Bourrier, V., Wheatley, P. J., & et al. 2015, Nature, 522, 459
Estrela, R., Swain, M. R., Roudier, G. M., et al. 2021, AJ, 162, 91
Fossati, L., Guilluy, G., Shaikhislamov, I. F., et al. 2022, A&A, 658, A136
Fossati, L., Pillitteri, I., Shaikhislamov, I. F., et al. 2023, A&A, 673, A37
Fouqué, P., Moutou, C., Malo, L., et al. 2018, MNRAS, 475, 1960
Fraine, J. D., Deming, D., Benneke, B., & et al. 2014, Nature, 513, 526
Fulton, B. J., & Petigura, E. A. 2018, AJ, 156, 264
Fulton, B. J., Petigura, E. A., Howard, A. W., et al. 2017, AJ, 154, 109
Gaia Collaboration (Brown, A., et al.) 2018, A&A, 616, A1
García Muñoz, A., & Schneider, P. C. 2019, ApJ, 884, L43
Giacobbe, P., Brogi, M., Gandhi, S., et al. 2021, Nature, 592, 205
Gillon, M., Pont, F., Demory, B. O., et al. 2007, A&A, 472, L13
Guilluy, G., Andretta, V., Borsa, F., et al. 2020, A&A, 639, A49
Guilluy, G., Giacobbe, P., Carleo, I., et al. 2022, A&A, 665, A104
Guilluy, G., Bourrier, V., Jaziri, Y., et al. 2023, A&A, 676, A130
Gully-Santiago, M., Morley, C. V., Luna, J., et al. 2024, AJ, 167, 142
Huang, C., Koskinen, T., Lavvas, P., & Fossati, L. 2023, ApJ, 951, 123
Hunter, A., Macgregor, A. B., Szabo, T. O., Wellington, C. A., & Bellgard, M. I. 2012, Source Code Biol. Med., 7, 1
Johnstone, C. P., & Güdel, M. 2015, A&A, 578, A129
Johnstone, C. P., Bartel, M., & Güdel, M. 2021, A&A, 649, A96
Kass, R. E., & Raftery, A. E. 1995, J. Am. Statis. Assoc., 90, 773
Kausch, W., Noll, S., Smette, A., et al. 2015, A&A, 576, A78
Khalafinejad, S., Molaverdikhani, K., Blecic, J., et al. 2021, A&A, 656, A142
Kirk, J., Alam, M. K., López-Morales, M., & Zeng, L. 2020, AJ, 159, 115
Knutson, H. A., Fulton, B. J., Montet, B. T., et al. 2014, ApJ, 785, 126
Kokori, A., Tsiaras, A., Edwards, B., et al. 2023, ApJS, 265, 4
Kosiarek, M. R., Crossfield, I. J. M., Hardegree-Ullman, K. K., et al. 2019, AJ, 157, 97
Kreidberg, L., Line, M. R., Thorngren, D., Morley, C. V., & Stevenson, K. B. 2018, ApJ, 858, L6

Krishnamurthy, V., Hirano, T., Gaidos, E., et al. 2023, MNRAS, 521, 1210
Kuckartz, U., R.adiker, S., Ebert, T., & Julia, S. 2013, Statistik: Eine verstandliche Einfuhrung, 2nd edn. (Wiesbaden: Springer Fachmedien)
Kulow, J. R., France, K., Linsky, J., & Loyd, R. O. P. 2014, ApJ, 786, 132
Langeveld, A. B., Madhusudhan, N., & Cabot, S. H. C. 2022, MNRAS, 514, 5192
Lanotte, A. A., Gillon, M., Demory, B. O., et al. 2014, A&A, 572, A73
Lavie, B., Ehrenreich, D., Bourrier, V., et al. 2017, A&A, 605, L7
Lecavelier Des Etangs, A. 2007, A&A, 461, 1185
Lovis, C., Dumusque, X., Santos, N. C., et al. 2011, arXiv e-prints [arXiv:1107.5325]
Lundkvist, M. S., Kjeldsen, H., Albrecht, S., et al. 2016, Nat. Commun., 7, 11201
Mamajek, E. E., & Hillenbrand, L. A. 2008, ApJ, 687, 1264
Mansfield, M., Bean, J. L., Oklopčić, A., et al. 2018, ApJ, 868, L34
Morello, G., Claret, A., Martin-Lagarde, M., et al. 2020, AJ, 159, 75
Nail, F., Oklopčić, A., & MacLeod, M. 2024, A&A, 684, A20
Nascimbeni, V., Piotto, G., Pagano, I., et al. 2013, A&A, 559, A32
Ninan, J. P., Stefansson, G., Mahadevan, S., et al. 2020, ApJ, 894, 97
Nortmann, L., Pallé, E., Salz, M., et al. 2018, Science, 362, 1388
Noyes, R. W., Weiss, N. O., & Vaughan, A. H. 1984, ApJ, 287, 769
Oklopčić, A. 2019, ApJ, 881, 133
Oklopčić, A., & Hirata, C. M. 2018, ApJ, 855, L11
Oliva, E., Origlia, L., Baffa, C., et al. 2006, SPIE Conf. Ser., 6269, 626919
Oliva, E., Origlia, L., Maiolino, R., et al. 2013, A&A, 555, A78
Palle, E., Nortmann, L., Casasayas-Barris, N., et al. 2020, A&A, 638, A61
Poppenhaeger, K. 2022, MNRAS, 512, 1751
Rainer, M., Harutyunyan, A., Carleo, I., et al. 2018, SPIE Conf. Ser., 10702, 1070266
Rumenskikh, M. S., Khodachenko, M. L., Shaikhislamov, I. F., et al. 2023, MNRAS, 526, 4120
Salz, M., Czesla, S., Schneider, P. C., et al. 2018, A&A, 620, A97
Sanz-Forcada, J. 2022, Astron. Nachr., 343, e20008
Seager, S., & Sasselov, D. D. 2000, ApJ, 537, 916
Sicilia, D., Malavolta, L., Pino, L., et al. 2022, A&A, 667, A19
Smette, A., Sana, H., Noll, S., et al. 2015, A&A, 576, A77
Spake, J. J., Sing, D. K., Evans, T. M., et al. 2018, Nature, 557, 68
Spake, J. J., Oklopčić, A., & Hillenbrand, L. A. 2021, AJ, 162, 284
Spinelli, R., Gallo, E., Haardt, F., et al. 2023, AJ, 165, 200
Stassun, K. G., Collins, K. A., & Gaudi, B. S. 2017, AJ, 153, 136
Stefànsson, G., Mahadevan, S., Petrovich, C., et al. 2022, ApJ, 931, L15
Stevenson, K. B., Harrington, J., Nymeyer, S., & et al. 2010, Nature, 464, 1161
Suárez Mascareño, A., Rebolo, R., González Hernández, J. I., & Esposito, M. 2015, MNRAS, 452, 2745
Szabó, G. M. & Kiss, L. L. 2011, ApJ, 727, L44
Ter Braak, C. J. F. 2006, Stat. Comput., 16, 239
Triaud, A. H. M. J., Gillon, M., Ehrenreich, D., et al. 2015, MNRAS, 450, 2279
Tsiaras, A., Waldmann, I. P., Zingales, T., et al. 2018, AJ, 155, 156
Turner, J. D., Pearson, K. A., Biddle, L. I., et al. 2016, MNRAS, 459, 789
Tyler, D., Petigura, E. A., Oklopčić, A., & David, T. J. 2024, ApJ, 960, 123
Vidal-Madjar, A., Lecavelier des Etangs, A., Désert, J. M., et al. 2003, Nature, 422, 143
Vidal-Madjar, A., Désert, J. M., Lecavelier des Etangs, A., et al. 2004, ApJ, 604, L69
Vissapragada, S., Knutson, H. A., Jovanovic, N., et al. 2020, AJ, 159, 278
Vissapragada, S., Knutson, H. A., Greklek-McKeon, M., et al. 2022, AJ, 164, 234
Yan, F., Pallé, E., Fosbury, R. A., Petr-Gotzens, M. G., & Henning, T. 2017, A&A, 603, A73
Zhang, M., Dai, F., Bean, J. L., Knutson, H. A., & Rescigno, F. 2023, ApJ, 953, L25

[1] INAF – Osservatorio Astrofisico di Torino, Via Osservatorio 20, 10025, Pino Torinese, Italy
e-mail: gloria.guilluy@inaf.it
[2] INAF – Osservatorio Astronomico di Palermo, Piazza del Parlamento, 1, 90134 Palermo, Italy
[3] University of Palermo, Department of Physics and Chemistry – Emilio Segrè, Via Archirafi 36, Palermo, Italy
[4] DISAT, Università degli Studi dell'Insubria, Via Valleggio 11, 22100 Como, Italy
[5] INAF – Osservatorio Astronomico di Brera, Via E. Bianchi 46, 23807 Merate, Italy
[6] Space Research Institute, Austrian Academy of Sciences, Schmiedlstrasse 6, 8042 Graz, Austria
[7] INAF – Osservatorio Astrofisico di Catania, Via S. Sofia 78, 95123 Catania, Italy
[8] Fundación Galileo Galilei-INAF, Rambla José Ana Fernandez Pérez 7, 38712 Breña Baja, TF, Spain
[9] INAF – Osservatorio Astronomico di Roma, Via Frascati 33, 00078 Monte Porzio Catone, Italy
[10] INAF – Osservatorio Astronomico di Trieste, Via Tiepolo 11, 34143 Trieste
[11] Instituto de Astrofísica de Canarias (IAC), Calle Vía Láctea s/n, 38200 La Laguna, Tenerife, Spain
[12] Departamento de Astrofísica, Universidad de La Laguna (ULL), 38206 La Laguna, Tenerife, Spain
[13] INAF – Osservatorio Astronomico di Padova, Vicolo dell'Osservatorio 5, 35122 Padova, Italy
[14] Dipartimento di Fisica e Astronomia Galileo Galilei, Università di Padova, Vicolo dell'Osservatorio 3, 35122 Padova, Italy
[15] Department of Physics, University of Rome "Tor Vergata", Via della Ricerca Scientifica 1, 00133 Roma, Italy
[16] Max Planck Institute for Astronomy, Königstuhl 17, 69117 Heidelberg, Germany
[17] INAF – Osservatorio Astrofisico di Arcetri, Largo E. Fermi 5, 50125 Firenze, Italy

Appendix A: Additional figures and tables

Table A.1: Adopted parameters.

Parameter	Value	Reference
WASP-69		
Stellar Parameters		
Spectral type	K5	Anderson et al. (2014)
Stellar mass, $M_\star$ [$M_\odot$]	0.826 ± 0.029	Anderson et al. (2014)
Stellar radius, $R_\star$ [$R_\odot$]	0.813 ± 0.028	Anderson et al. (2014)
Effective temperature, T_{eff} [K]	4715 ± 50	Anderson et al. (2014)
Metallicity, [Fe/H] [dex]	0.144 ± 0.077	Anderson et al. (2014)
log $g_\star$ (log$_{10}$[cm s^{-2}])	4.535 ± 0.023	Anderson et al. (2014)
Systemic velocity, v_{sys} (km s^{-1})	-9.37 ± 0.20	Gaia DR2 (Gaia Collaboration 2018)
Magnitude (J-band)	8.032 ± 0.023	Cutri et al. (2003)
WASP-69b Parameters		
Orbital period, P [days]	3.86813888 ± 9.1e-07	Kokori et al. (2023)
Transit epoch, T_0 [BJD$_{TDB}$]	2457269.01322 ± 0.00027	Kokori et al. (2023)
Eccentricity, e	0 (fixed)	Anderson et al. (2014)
Argument of periastron, ω [deg]	90(fixed)	
Stellar reflex velocity, $K_\star$ [m s^{-1}]	38.1 ± 2.4	Anderson et al. (2014)
Orbital major semi-axis, a [au]	0.04525 ± 0.00053	Anderson et al. (2014)
Orbital inclination, i [deg]	86.71 ± 0.20	Anderson et al. (2014)
Planetary mass, M_{pl}	0.260 ± 0.017	Anderson et al. (2014)
Planetary radius, R_{pl} [R_{jup}]	1.057 ± 0.047	Anderson et al. (2014)
Impact parameter, b	0.686 ± 0.023	Anderson et al. (2014)
Equilibrium temperature, T_{eq} [K]	963 ± 18	Anderson et al. (2014)
Planet radial-velocity semi-amplitude, K_p [m s^{-1}]	127.1 ± 1.5	This paper [2]
WASP-107		
Stellar Parameters		
Spectral type	K6	Anderson et al. (2017)
Stellar mass, $M_\star$ [$M_\odot$]	0.69 ± 0.05	Anderson et al. (2017)
Stellar radius, $R_\star$ [$R_\odot$]	0.66 ± 0.02	Anderson et al. (2017)
Effective temperature, T_{eff} [K]	4430 ± 120	Anderson et al. (2014)
Metallicity, [Fe/H] [dex]	0.020 ± 0.100	Anderson et al. (2014)
log $g_\star$ (log$_{10}$[cm s^{-2}])	4.5 ± 0.1	Anderson et al. (2014)
Systemic velocity, v_{sys} [km s^{-1}]	13.74 ± 0.31	Gaia DR2 (Gaia Collaboration 2018)
Magnitude (J-band)	9.378 ± 0.021	Cutri et al. (2003)
WASP-107b Parameters		
Orbital period, P [days]	5.72148926 ± 8.5e-07	Kokori et al. (2023)
Transit epoch, T_0 [BJD$_{TDB}$]	2457515.672118 ± 7.5e-05	Kokori et al. (2023)
Eccentricity, e	0 (fixed)	Anderson et al. (2017)
Argument of periastron, ω [deg]........	90 (adopted)	
Stellar reflex velocity, $K_\star$ (m s^{-1})	17 ± 2	Anderson et al. (2017)
Orbital major semi-axis, a [au]	0.055 ± 0.001	Anderson et al. (2017)
Orbital inclination, i [deg]	89.7 ± 0.2	Anderson et al. (2017)
Planetary mass, M_{pl} [M_{jup}]	0.12 ± 0.01	Anderson et al. (2017)
Planetary radius, R_{pl} [R_{jup}]	0.94 ± 0.02	Anderson et al. (2017)
Impact parameter, b	0.09 ± 0.07	Anderson et al. (2017)
Equilibrium temperature, T_{eq} [K]	770 ± 60	Anderson et al. (2014)
Planet radial-velocity semi-amplitude, K_p [m s^{-1}]	105.2 ± 2.5	This paper [2]
HAT-P-11		
Stellar Parameters		
Spectral type	K4 V	Bakos et al. (2010)
Stellar mass, $M_\star$ [$M_\odot$]	0.86 ± 0.06	Lundkvist et al. (2016)
Stellar radius, $R_\star$ [$R_\odot$]	0.76 ± 0.01	Lundkvist et al. (2016)
Effective temperature, T_{eff} [K]	4780 ± 50	Bakos et al. (2010)
Metallicity, [Fe/H] [dex]	0.31 ± 0.05	Bakos et al. (2010)

Table A.1: Continued.

Parameter	Value	Reference
log $g_\star$ ($\log_{10}[\mathrm{cm\,s^{-2}}]$)	4.37 ± 0.22	Stassun et al. (2017)
Systemic velocity, v_sys [km s^{-1}]	-63.24 ± 0.26	Gaia DR2 (Gaia Collaboration 2018)
Magnitude (J-band)	7.608 ± 0.029	Cutri et al. (2003)
HAT-P-11b Parameters		
Orbital period, P [days]	$4.88780201 \pm 1.7\mathrm{e}{-07}$	Kokori et al. (2023)
Transit epoch, T_0 [BJD$_\mathrm{TDB}$]	$2455798.515261 \pm 2.3\mathrm{e}{-05}$	Kokori et al. (2023)
Eccentricity, e	$0.2577^{+0.0033}_{-0.0025}$	Basilicata et al. (2024)
Argument of periastron, ω [deg]	$19.0^{+2.9}_{-3.0}$	Basilicata et al. (2024)
Stellar reflex velocity, $K_\star$ [m s^{-1}]	11.21 ± 0.36	Basilicata et al. (2024)
Orbital major semi-axis, a [au]	0.0532 ± 0.0010	Basilicata et al. (2024)
Orbital inclination, i [deg]	89.027 ± 0.068	Basilicata et al. (2024)
Planetary mass, M_pl [M_jup]	0.0818 ± 0.0046	Basilicata et al. (2024)
Planetary radius, R_pl [R_jup]	0.4466 ± 0.0059	Basilicata et al. (2024)
Impact parameter, b	$0.227^{+0.013}_{-0.015}$	Basilicata et al. (2024)
Equilibrium temperature T_eq [K]	847^{+46}_{-54}	Basilicata et al. (2024)
Planet radial-velocity semi-amplitude, K_p [m s^{-1}]	123.5 ± 2.9	This paper [2]
GJ436		
Stellar Parameters		
Spectral type	M2.5V	Butler et al. (2004)
Stellar mass, $M_\star$ [$M_\odot$]	$0.556^{+0.071}_{-0.065}$	Lanotte et al. (2014)
Stellar radius, $R_\star$ [$R_\odot$]	0.455 ± 0.018	Lanotte et al. (2014)
Effective temperature, T_eff [K]	3416 ± 100	Lanotte et al. (2014)
Metallicity, [Fe/H] [dex]	0.02 ± 0.20	Lanotte et al. (2014)
log $g_\star$ ($\log_{10}[\mathrm{cm\,s^{-2}}]$)	4.843 ± 0.018	Lanotte et al. (2014)
Systemic velocity, v_sys [km s^{-1}]	9.59 ± 0.0008	Fouqué et al. (2018)
Magnitude (J-band)	6.900 ± 0.024	Cutri et al. (2003)
GJ436b Parameters		
Orbital period, P [days]	$2.643897621 \pm 9.6\mathrm{e}{-08}$	Kokori et al. (2023)
Transit epoch, T_0 (BJD$_\mathrm{TT}$)	$2455290.751684 \pm 5.2\mathrm{e}{-05}$	Kokori et al. (2023)
Eccentricity, e	$0.1616^{0.0041}_{-0.0032}$	Lanotte et al. (2014)
Argument of periastron, ω [deg]	$327.2^{+1.8}_{-2.2}$	Lanotte et al. (2014)
Stellar reflex velocity, $K_\star$ [m s^{-1}]	17.59 ± 0.25	Lanotte et al. (2014)
Orbital major semi-axis, a [au]	$0.0308^{+0.0013}_{-0.0012}$	Lanotte et al. (2014)
Orbital inclination, i [deg]	$86.858^{+0.049}_{-0.052}$	Lanotte et al. (2014)
Planetary mass, M_pl [M_jup]	$0.080^{+0.007}_{-0.006}$	Lanotte et al. (2014)
Planetary radius, R_pl [R_jup]	0.366 ± 0.014	Lanotte et al. (2014)
Impact parameter, b	$0.7972^{+0.0053}_{-0.0055}$	Lanotte et al. (2014)
Equilibrium temperature T_eq [K]	686 ± 10	Turner et al. (2016)
Planet radial-velocity semi-amplitude, K_p [m s^{-1}]	$128.1^{+5.5}_{-5.0}$	This paper [2]
GJ3470		
Stellar Parameters		
Spectral type	M1.5	Kosiarek et al. (2019)
Stellar mass, $M_\star$ [$M_\odot$]	0.51 ± 0.06	Kosiarek et al. (2019)
Stellar radius, $R_\star$ [$R_\odot$]	0.48 ± 0.04	Kosiarek et al. (2019)
Effective temperature, T_eff [K]	3652 ± 50	Kosiarek et al. (2019)
Metallicity, [Fe/H] [dex]	0.20 ± 0.10	Kosiarek et al. (2019)
log $g_\star$ ($\log_{10}[\mathrm{cm\,s^{-2}}]$)	4.658 ± 0.035	Kosiarek et al. (2019)
Systemic velocity, v_sys [km s^{-1}]	26.09 ± 0.25	Gaia DR2 (Gaia Collaboration 2018)
Magnitude (J-band)	8.794 ± 0.026	Cutri et al. (2003)
GJ3470b Parameters		
Orbital period, P [days]	$3.33665266^{+0.0000003}_{-0.0000003}$	Stefànsson et al. (2022)
Transit epoch, T_0 [BJD$_\mathrm{TDB}$]	$2456340.72559^{+0.00011}_{-0.0001}$	Stefànsson et al. (2022)
Eccentricity, e	$0.125^{+0.043}_{-0.042}$	Stefànsson et al. (2022)
Argument of periastron, ω [deg]	$-83.4^{+3.4}_{-1.7}$	Stefànsson et al. (2022)

Table A.1: Continued.

Parameter	Value	Reference
Stellar reflex velocity, $K_\star$ [m s^{-1}]	$8.03^{+0.38}_{-0.37}$	Stefànsson et al. (2022)
Orbital major semi-axis, a [au]	$0.0288^{+0.0029}_{-0.0028}$	derived from Kosiarek et al. (2019)
Orbital inclination, i [deg]	$88.88^{+0.62}_{-0.45}$	Biddle et al. (2014)
Planetary mass, M_{pl} [M_{jup}]	$0.03958^{+0.00412}_{-0.00403}$	Kosiarek et al. (2019)
Planetary radius, R_{pl} [R_{jup}]	0.346 ± 0.029	Kosiarek et al. (2019)
Impact parameter, b	0.29 ± 0.14	Biddle et al. (2014)
Equilibrium temperature T_{eq} [K]	604 ± 98	Biddle et al. (2014)
Planet radial-velocity semi-amplitude, K_p [m s^{-1}]	114.7 ± 0.5	This paper [2]

Notes, $K_{pl} = \frac{2\pi a}{P} \frac{\sin i}{\sqrt{1-e^2}} = \left(\frac{2\pi G}{P}\right)^{\frac{1}{3}} \frac{(M_\star + M_{pl})^{\frac{1}{3}} \sin i}{\sqrt{1-e^2}}$.
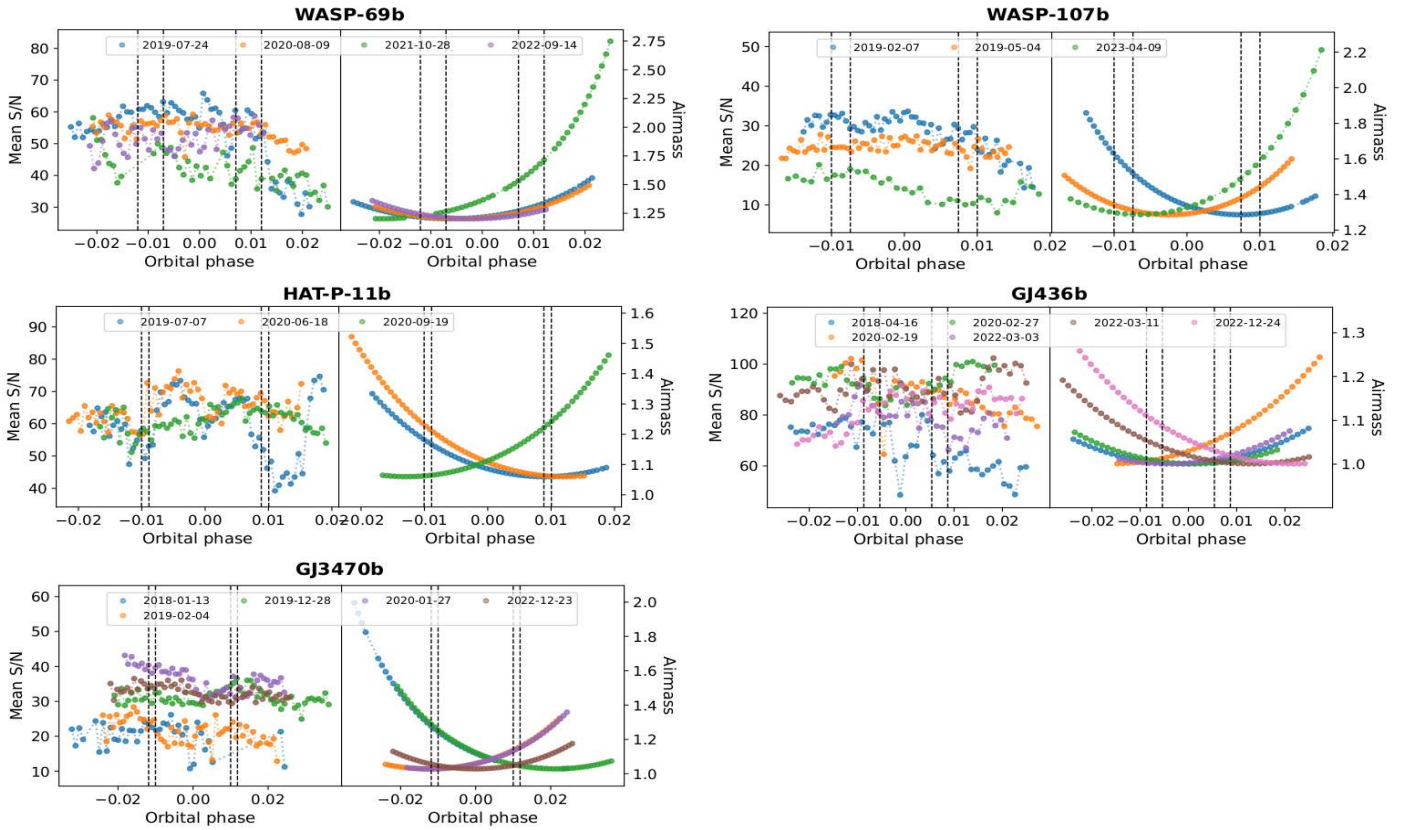

Fig. A.1. S/N in the region of interest (1082.49-1085.5 nm; left panel) and airmass (right panel) measured during the GIANO-B observations for each investigated target. The vertical dashed lines mark the t_1, t_2, t_3, and t_4 contact points (from left to right). The dashed green line for WASP-107b indicates the transit we had to discard for adverse seeing conditions.
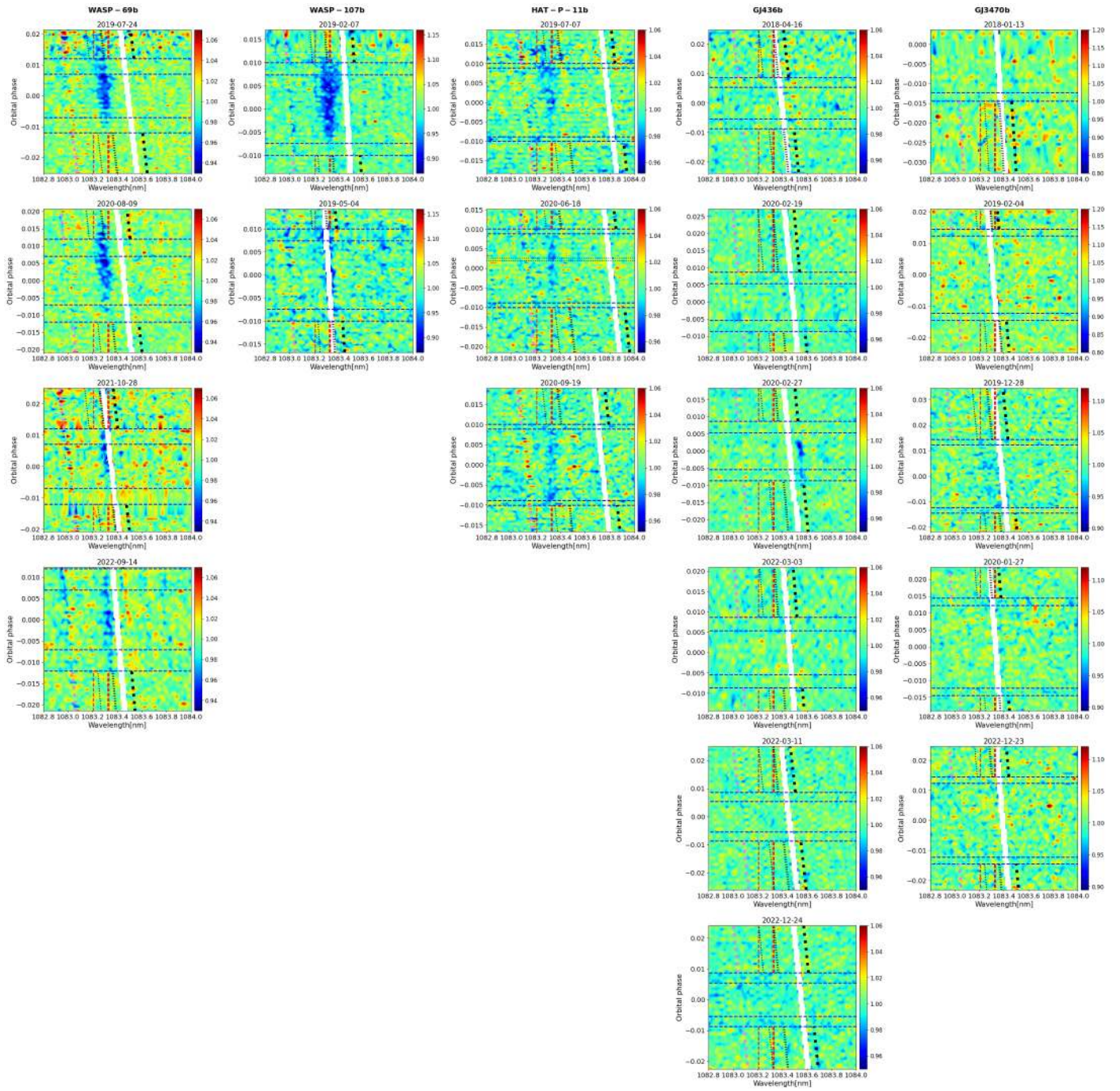
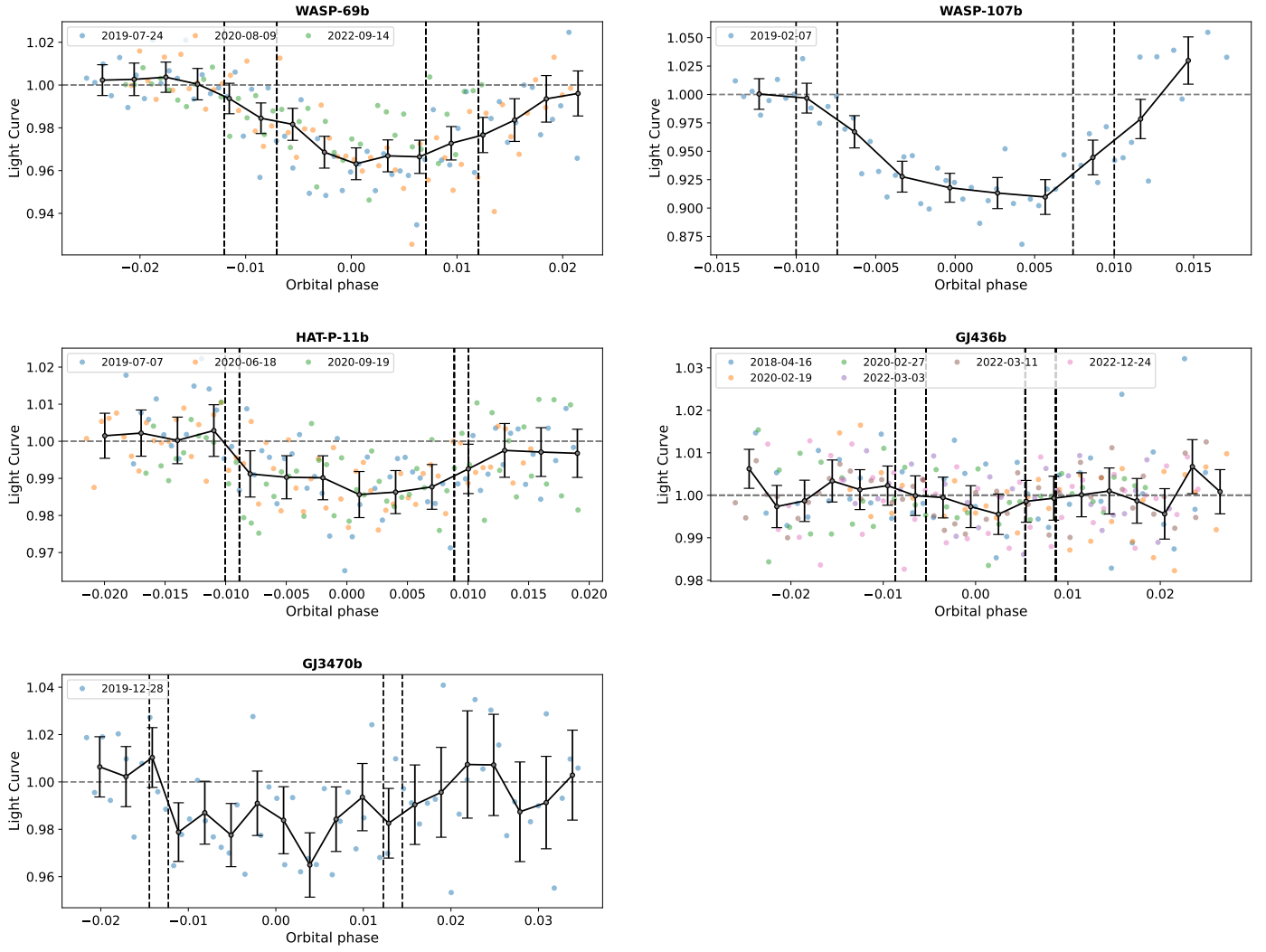**Fig. A.2.** Same as Fig. 3 but for all the investigated nights.

Fig. A.3. Transmission light curve of He I in the planetary rest frame for the investigated targets. The vertical dashed lines mark the t_1, t_2, t_3, and t_4 contact points (from left to right). The grey horizontal dashed line is the continuum level.

Table A.2: Priors used in the DE-MCMC analysis.

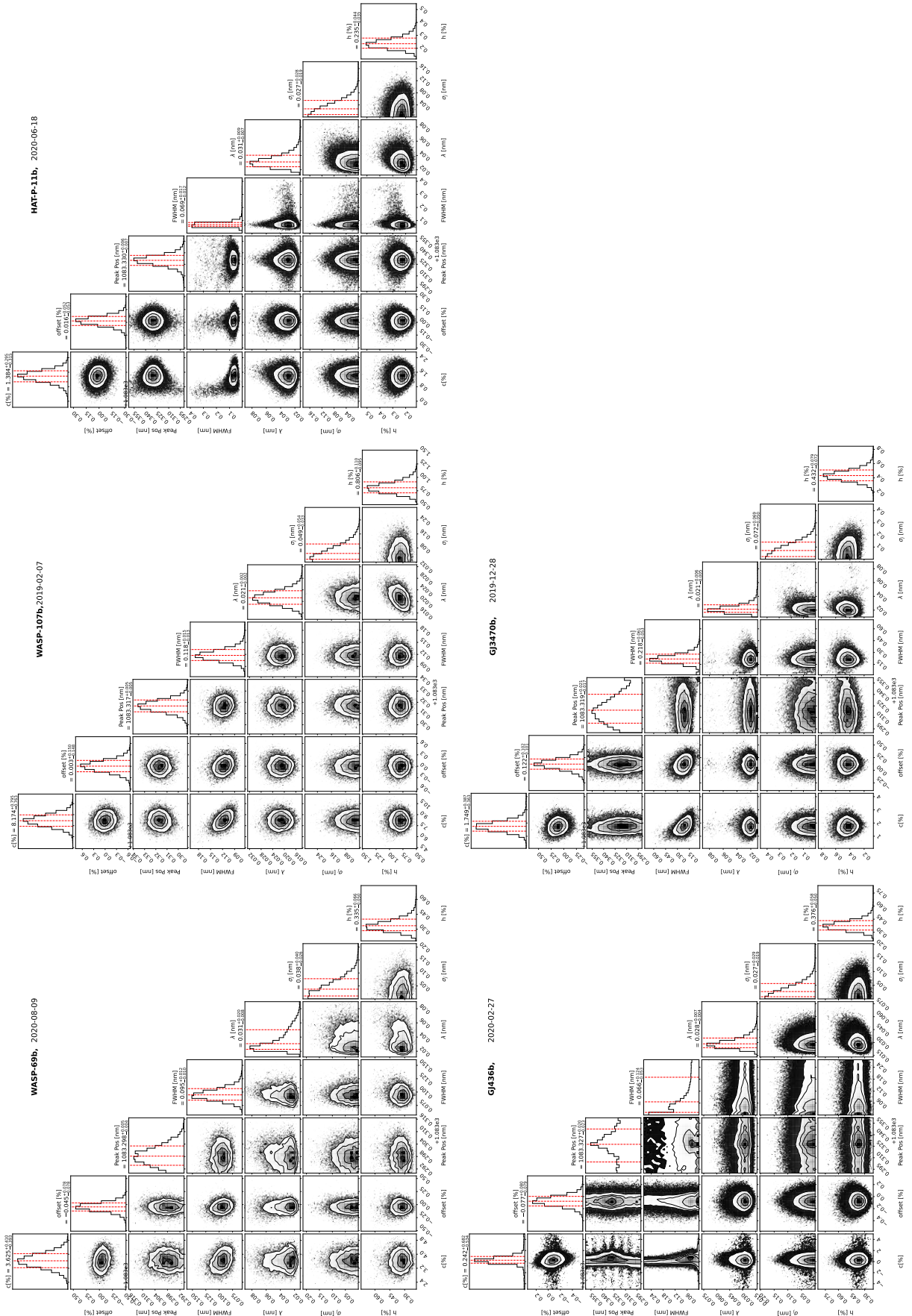| Value	Priors
Peak Pos$_{gauss}$ [nm]	U[1083.29,1083.36]
σ_{jit}	U[0,+∞]
Ampl [%]	U[0,3]
λ [nm]	U[0.01,0.09]

Fig. A.4. Example of the posterior distribution of the investigated parameters in the DE-MCMC analysis. The excess of absorption c [%], offset [%], peak position, and FWHM correspond to the parameters we used in the Gaussian fit, while the jitter term σ_j, the semi-amplitude of the correlated noise h, the correlation length λ were used to parametrise the SE kernel within the GP. The larger FWHM for GJ 3470 b is believed to be attributed to residuals from OH line contamination.

Table A.3: Result night by night.

	Night	Peak position [nm]	Excess of absorption c [%]	FWHM [nm]	Significance [σ]
WASP-69b	24 July 2019	$1083.2974^{+0.0032}_{-0.0031}$	$4.31^{+0.30}_{-0.31}$	$0.0960^{+0.008}_{-0.006}$	14.2
	09 August 2020	$1083.2982^{+0.0049}_{-0.0044}$	$3.63^{+0.41}_{-0.39}$	$0.0948^{+0.012}_{-0.010}$	9.0
	14 September 2022	$1083.3187^{+0.0069}_{-0.0073}$	$3.14^{+0.54}_{-0.55}$	$0.0764^{+0.015}_{-0.010}$	5.8
WASP-107b	07 February 2019	$1083.3167^{+0.0053}_{-0.0052}$	$8.17^{+0.80}_{-0.76}$	$0.1176^{+0.015}_{-0.013}$	10.5
HAT-P-11b	07 July 2019	$1083.3189^{+0.0092}_{-0.0098}$	$1.35^{+0.27}_{-0.27}$	$0.1059^{+0.023}_{-0.018}$	4.9
	18 June 2020	$1083.3302^{+0.0064}_{-0.0066}$	$1.38^{+0.29}_{-0.31}$	$0.0686^{+0.017}_{-0.012}$	4.5
	19 September 2020	$1083.3271^{+0.0085}_{-0.0088}$	$1.35^{+0.31}_{-0.32}$	$0.0829^{+0.018}_{-0.015}$	4.3
GJ436b	16 April 2018		<0.24(0.34)		
	19 February 2020		<0.34(0.44)		
	27 February 2020		<0.52(0.66)		
	03 March2023		<0.38(0.52)		
	11 March2023		<0.63(0.68)		
	24 December 2022		<0.39(0.45)		
GJ3470b	28 December 2019	$1083.3194^{+0.0207}_{-0.0170}$	$1.75^{+0.39}_{-0.36}$	$0.2180^{+0.061}_{-0.053}$	4.7
	23 December 2022		<0.10(0.22)		

Notes. From left to right: the investigated night, the peak position, excess of absorption, and FWHM obtained from the DE-MCMC analysis, and the significance of the detection. The upper limits are reported at 1σ and at 2σ (in brackets).
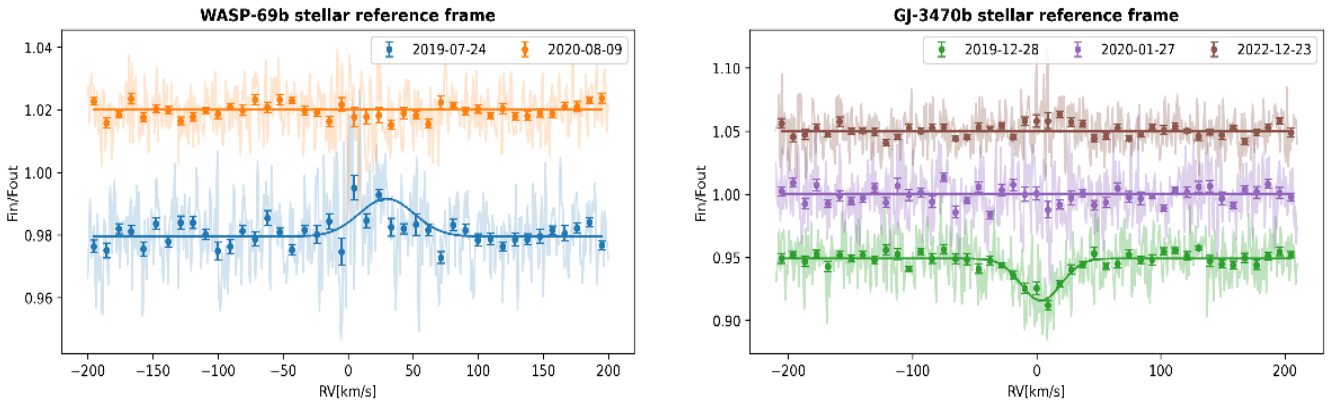

Fig. A.5. Weighted average of the full in-transit spectra in the star rest frame for WASP-69b (left panel) and GJ3470b (right panel) centred on the Hα line. Light colours indicate the not binned transmission spectra, while dots show the transmission spectra binned $20\times$ (in RV). The overplotted fit is performed on the not-binned spectra and represents the model favourite by the BIC test.

Table A.4: $\log R'_{HK}$ values.

	Night	$\log R'_{HK}$
HD189733b	30 May 2017	-4.461 ± 0.006
	19 June 2017	-4.546 ± 0.005
	20 July 2017	-4.499 ± 0.006
	29 July 2017	-4.500 ± 0.005
	18 October 2018	-4.509 ± 0.003
	all	-4.502 ± 0.029
WASP-80b	9 August 2019	-3.836 ± 0.015
	21 September 2019	-3.870 ± 0.010
	26 June 2020	-3.859 ± 0.016
	17 September 2020	-3.846 ± 0.068
	all	-3.853 ± 0.037
WASP-69b	24 July 2019	-4.561 ± 0.008
	09 August 2020	-4.571 ± 0.007
	28 October 2021	-4.608 ± 0.006
	all	-4.567 ± 0.011
WASP-107b	07 February 2019	-4.431 ± 0.017
	04 May 2019	-4.488 ± 0.015
	all	-4.461 ± 0.032
HAT-P-11b	07 July 2019	-4.712 ± 0.008
	18 June 2020	-4.675 ± 0.005
	19 September 2020	-4.700 ± 0.008
	all	-4.696 ± 0.017
GJ3470b	13 January 2018	-4.814 ± 0.092
	04 February 2019	-4.787 ± 0.078
	28 December 2019	-4.795 ± 0.019
	27 January 2020	-4.815 ± 0.019
	23 December 2022	-4.842 ± 0.013
	all	-4.809 ± 0.054
GJ436b	16 April 2018	-5.223 ± 0.028
	19 February 2020	-5.183 ± 0.010
	27 February 2020	-5.173 ± 0.018
	11 March 2023	-5.182 ± 0.015
	24 December 2022	-5.199 ± 0.015
	all	-5.191 ± 0.024
HAT-P-3b	29 January 2020	-4.896 ± 0.128

Notes. The $\log R'_{HK}$ measurements have been obtained from the CaII H&K lines through the offline version of HARPS-N DRS available through the Yabi web application (Hunter et al. 2012).[º] For GJ436 and GJ3470, which have an index colour B-V>1.1, we applied the Suárez Mascareño et al. (2015) formalism.